ACCEPTED MANUSCRIPT

Energy Level Alignment at Cobalt Phosphate/Electrolyte Interface:
Intrinsic Stability vs. Interfacial Chemical Reactions in 5 V Lithium Ion Batteries

SCHOLARONE™
Manuscripts

Energy Level Alignment at Cobalt Phosphate/Electrolyte Interface:
Intrinsic Stability vs. Interfacial Chemical Reactions in 5 V Lithium Ion Batteries

Gennady Cherkashinin [a,*], Robert Eilhardt,[a] Silvia Nappini,[b] Matteo Cococcioni,[c] Igor Píš,[b,d] Simone dal Zilio,[b]

Federica Bondino,[b] Nicola Marzari,[e] Elena Magnano[b,f] and Lambert Alff [a]

[a] Institute of Materials Science, Technische Universität Darmstadt, Alarich-Weiss-Str. 2, D-64287 Darmstadt, Germany
[b] IOM CNR Laboratorio TASC, Strada Statale 14, km. 163,5 in Area Science Park, 34149 Basovizza, Trieste, Italy
[c] Physics Department, University of Pavia, Via Bassi 6, I-27100 Pavia, Italy
[d] Elettra - Sincrotrone Trieste S.C.p.A., Basovizza, TS, Italy
[e] Theory and Simulation of Materials (THEOS), and National Centre for Computational Design and Discovery of Novel Materials (MARVEL), Ecole Polytechnique Federale de Lausanne (EPFL), CH-1015 Lausanne, Switzerland
[f] Department of Physics, University of Johannesburg, PO Box 524, Auckland Park, 2006, Johannesburg, South Africa

ABSTRACT: The intrinsic stability of the 5V $LiCoPO_4$ - $LiCo_2P_3O_{10}$ thin film (carbon free) cathode material coated with MoO_3 thin layer is studied by comprehensive synchrotron electron spectroscopy in-situ approach combined with first principle calculations. The atomic-molecular level study demonstrates fully reversible electronic properties of the cathode after the 1st electrochemical cycle. The polyanionic oxide is not involved into chemical reactions with the fluoroethylene containing liquid electrolyte even when being charged to 5.1 V vs. Li^+/Li. The high stability of the cathode is explained on the base of the developed energy level model. In contrast, chemical composition of the cathode-electrolyte interface evolves continuously by involving MoO_3 in the decomposition reaction with consequent leaching of oxide from the surface. The proposed mechanisms of chemical reactions are attributed to an external electrolyte oxidation via charge transfer from the relevant electron level to the MoO_3 valence band state, as well as to an internal electrolyte oxidation via proton transfer to the solvents. This study gives deeper inside into the development of both a doping strategy to enhance electronic conductivity of high voltage cathode materials, and an efficient surface coating against unfavorable interfacial chemical reactions.

Keywords: $LiCoPO_4$ 5V cathode material for Li-ion batteries, $LiCo_2P_3O_{10}$, MoO_3, electronic structure, SPES and XANES, DFT calculations

INTRODUCTION

A key trend in the modern development of next-generation Li-ion batteries (LIB) is an increase of the energy density and power density. Nowadays, there exist mostly two strategies to enhance the energy density, via an increase of the capacity of the electrodes (cathode and anode) or of the average voltage of the battery cell. Simultaneous enhancement of both the capacity and the voltage is practically not enforceable, since high capacity cathode materials have commonly a relatively low oxidation potential (Figure S1). A good example are Li-S or Li-air batteries with a theoretical capacity above 1500 A h/kg and operation voltage below 3.0 V (Figure S1,a).[1,2] In this regard, not much attention is paid to high voltage cathodes above 4.8 V (vs. Li^+/Li) oxidation potential (Figure S1,b), This a skepticism is mostly associated to chemical (or electrochemical) instability of the liquid and solid electrolytes,[3,4] as well as to the irreversible changes of crystal structure of the cathode materials at a deep stage of delithiation. For $Li[Ni,Mn,Co]O_2$ layered and LiM_2O_4 spinel oxides, the structural collapse can be expected at > 5.0 V operation voltage. Olivine structure phosphates attracted the attention primarily due to an exceptional electrochemical performance of olivine $LiFePO_4$,[5] In contrast to layered oxides, which loose irreversibly oxygen during deep cycling, olivine structure is structurally and chemically robust due to the PO_4 polyanion which stabilizes the lattice oxygen. $LiCoPO_4$ and $LiNiPO_4$ have the highest oxidation potential among all olivine phosphates family and, therefore, deliver the highest theoretical energy density. Unfortunately, the sluggish kinetics of M^{2+}/M^{3+} (M= Co, Ni) transition during Li^+ de/insertion coupled to extremely low intrinsic electronic conductivity is the reason of much lower practical capacity of the $LiMPO_4$ family with respect to other cathode materials. Carbon coating is the cheapest way to enhance electronic conductivity.[6] However, carbon is oxidized at high operation voltage (> 4.8 V), triggered by water formation in carbonate containing electrolytes.[7] In addition, the coating does not increase electronic conductivity in the crystal lattice, but costs battery capacity due to a high carbon content (10 - 20% of total mass) in the composites.[8] Among other strategies to enhance both the Li^+ diffusion rate and electronic conductivity are doping and off-stoichiometric compositional variation.[8-14] More appealing could be the implementation of a secondary phase of a higher oxidation potential which forms a highly conductive network within the host. It would provide an additional gain in the energy density, which is a big challenge.

Besides the structural stability relevant to the bulk properties of cathodes,[15] physicochemical conditions at the

cathode-electrolyte interface (CEI) play a dominating role in the battery performance. The electrolyte decomposition is often accompanied by the involvement of cathode material in interfacial chemical reactions,[16] which lead to reduction of transition metals at the CEI.[17] The surface coating can protect the cathodes against unwanted reactions with electrolyte. However, such functionality might be contradicting for protective layers with high electronic conduction. The challenge to develop an effective coating stable above 4.8 V is probably the reason that only a few studies on $LiMPO_4$ (M= Co, Ni) coated with metal oxides (or vice versa) do exist.[18-21] MoO_3 coating of high voltage cathodes has attracted the attention because the former reduces electrolyte decomposition and impedes dissolution of transition metals in $LiNi_{0.5}Mn_{1.5}O_4$ and $LiNi_{0.5}Co_{0.2}Mn_{0.3}O_4$.[22,23] In addition, Mo doping leads to an increase of intrinsic electronic conductivity of various electrode materials and widens the one-dimensional diffusion channels for Li ions.[9,10,24] Unfortunately, the relevant researches were limited to 4.6 V charged state, whereas the detailed mechanisms explaining interfacial stability via Mo- coating/doping were not proposed. An improved understanding of interfacial conditions at the atomic-molecular level would give deeper insight into the stability (or instability) of artificial buffer layers at high voltage and therefore, allows to develop routes for material synthesis with optimal chemical composition and/or thickness of the protective layers.

Recently, we have shown that $LiCoPO_4$ (LCP) olivine type thin film cathode material tailored with $LiCo_2P_3O_{10}$ (LCPO) exhibits a very high electronic conductivity and high Li^+ ion diffusion rate without usage of conductive carbon.[25] Here, we apply a comprehensive in-situ depth resolved electron spectroscopy approach to demonstrate both the high intrinsic stability of LCP−LCPO cathode electrochemically cycled to the deepest stage of delithiation (5.1 V vs. Li^+/Li) and high catalytic activity of the MoO_6 coating layer towards fluorinated liquid electrolyte. The fully reversible electronic properties of LCP-LCPO, such as the oxidation states of Co, the Co 3d−O 2p hybridization, the density of occupied and unoccupied states near the Fermi level (E_F), the work function, ionization potential, etc., as well as the evolution of the interfacial chemical composition upon charging/discharging of the cathode, are evidenced by X-ray photoemission spectroscopy (PES) and X-ray absorption near edge spectroscopy (XANES). First principle calculations of the LCP-LCPO electronic structure were performed to model electrochemical behavior of the cathode, in particularly to evaluate the average voltage of the LCP- and LCPO- phases.

Scanning electron microscopy (SEM) and energy- dispersive X-ray spectroscopy (EDS) are applied to study surface morphology and lateral distribution of elements.

EXPERIMENTAL SECTION

Thin film growth of 5 V cathode material and the surface chemical analysis. The polycrystalline $LiCoPO_4$ thin film cathode materials with an average thickness of 700 nm were grown on Pt substrates by using radio-frequency (RF) sputtering of a $LiCoPO_4$ target material. The base pressure in the ultrahigh vacuum (UHV) chamber before film deposition was ~5×10^{-9} mbar. The films were preliminarily deposited at room temperature in argon (Ar) atmosphere (p_{Ar} ~1×10^{-2} mbar) followed by post-deposition annealing at 700° C in air. The power applied to the magnetrons was varied in the range of 1.3-2.5 Wcm^{-2}. The annealing was carried out by using a laser heating setup,[25] with a heating rate of 5 − 10° C/min and 30 min duration. Synthetic air (ALPHAGAZ™ 1 LUFT of 99.999 mol % purity, Air Liquide) was supplied to the UHV chamber during the film annealing. Stainless steel sample holders were used to hold the Pt substrates. The coating with MoO_3 was achieved upon the sample annealing in air (1 bar). Molybdenum contained in a stainless-steel alloy interacts with air forming highly volatile molybdenum oxides.[26] The adsorbed Mo atoms can also diffuse to the bulk of material, thereby playing a role as a dopant.[23] The chemical composition and electronic structure/ properties of the as prepared $LiCoPO_4$ films were firstly analyzed in-situ by photoelectron spectroscopy (XPS and UPS) in the Darmstadt Integrated System for Battery Research (DAISY-BAT). The analysis chamber (base pressure <5×10^{-9} mbar) is equipped with a PHI 5000 VersaProbe spectrometer (Physical Electronics), monochromatic Al Kα (hν=1486.7 eV), He I (21.2 eV) and He II (40.8 eV) ultra-violet sources. The binding energies of the spectra have been referenced to the Fermi level of a clean Ag-polycrystalline foil. A Mo content less than 3% on the $LiCoPO_4$ surface was determined by XPS.

Electrochemical Experiments. As prepared (pristine) $LiCoPO_4$ olivine-based cathode materials were transported to a glove-box (MBraun, Germany) for the battery cell assembling under argon atmosphere. A home-made transferable vacuum chamber was used for this purpose to avoid the sample contact with air. $LiCoPO_4$ olivine-based battery cells were charged/discharged to a selected potential in the 3.0 V- 5.1 V range

2

with a 0.1 mV/s scan rate in the cyclic voltammetry (CV) mode by using a potentiostat (VMP2 Princeton Applied Research, USA). A Swagelok-type two electrode cell was used. 1M $LiPF_6$ in 4:1 wt/wt Dimethyl Carbonate (DMC): Fluorinated Ethylene Carbonate (FEC) + 0.2%wt Trimethylboroxine (TMB) (Solvionic, France) was used as electrolyte. A metallic lithium foil was used as anode and Celgard®2500 as separator. The 3.0 V potential was chosen as reverse value of the discharged state for the electrochemical cycling range to ensure that no reduction of the electrolyte components occurs, taking into account the reduction potentials of the $LiPF_6$ salt, the DMC- and FEC- solvents, which are below 3 V vs. Li^+/Li.[3, 27] The $LiCoPO_4$ thin film cathodes at the charged states of 4.9 V, 5.1 V and at the discharged states of 4.9 V, 4.75 V, 4.6 V, 3.0 V vs. Li^+/Li were rinsed in DMC, dried upon Ar-atmosphere and afterwards loaded to the home-made UHV transferable chamber (DAISY-MOVE) equipped with a nonevaporable getter (NEG) pump, which maintains a pressure of $\sim 10^{-9}$ mbar. Finally, the samples were transported to Elettra (Trieste, Italy) for synchrotron radiation photoemission experiments. The electrochemical experiments were performed on several battery cells for a high reproducibility.

SPES and XAS experiments at Elettra Synchrotron. The DAISY-MOVE chamber delivered to the Elettra synchrotron facility was connected to the BACH beamline end-station, allowing the sample transfer under UHV conditions to the load-lock and afterwards to the measurement chamber. The quasi in-situ soft SPES, O K-, Co $L_{3,2}$-, Co $M_{3,2}$-, Li K- and P $L_{3,2}$- XANES spectra were measured with synchrotron radiation linearly polarised in the horizontal plane. The BACH beamline endstation is equipped with a VG-Scienta R3000 hemispherical analyser at an angle of 60° with respect to the incident beam direction. The photoemission spectra were acquired at normal emission geometry with a total energy resolution of 300 meV. The binding energies were referenced to the Fermi level of a clean Au polycrystalline foil in electric contact with the analyzed samples. The photoemission experiments were carried out by selecting suitable photon energies in order to collect photoelectrons with defined kinetic energies (E_{kin}) to provide the same probing depth for all core level- and valence band- electrons. The inelastic mean free path (IMFP) of electrons (λ) vs. the kinetic energy (E_{kin}) was estimated from the Tanuma, Powell, and Penn (TPP – 2M) formula.[28] A maximal surface and bulk sensitivity were achieved with $\lambda \sim 6$ Å and $\lambda \sim 27$ Å, respectively, which gives probing depth, $d_{XPS} = 3\lambda$, of ~20 Å and ~80 Å for the surface sensitive and

bulk related experiments, respectively. Thickness of MoO_3 layer on the LCP-LCPO surface is around 3 nm estimated according to the equation: $\quad d = \lambda \times Cos(\theta) \times ln\left[\frac{I(Mo3d)}{I(P2p)}\frac{N(LCP - LCPO)}{N(MoO3)} + 1\right].$ Here, I(Mo3d) and I(P2p) are the photoelectron intensities expressed as $I = \frac{I^{exp}}{\sigma \times \lambda \times T(E_{kin})}$ where I^{exp} is area of the Mo3d and P2p photoelectron spectra, respectively; $\sigma(h\nu)$ is the cross section of photoionization [Ref.[29]]; $T(E_{kin})$ is the transmission function of the spectrometer; $N = \frac{\rho \times N_A}{M}$, where N_A is the Avogadro constant, ρ is density, M is molar weight. The equation is valid for close kinetic energies of photoelectrons and when IMFPs from the substrate and a top layer are similar.

The energies of O K-, Co $L_{3,2}$-, P $L_{3,2}$- and Co $M_{3,2}$- XANES were calibrated with respect to the energies of incident photons by measuring the binding energies of the Au4f core-level or the E_F level of a clean gold foil. XANES spectra were recorded in total electron yield (TEY) mode by using a picommeter (Keithley 428 Current Amplifier) to measure the drain current on the sample. The Li K and Co $M_{3,2}$ XANES were acquired in total fluorescence yield (TFY). Such selection of the photon energies allows us to analyse the electronic properties over a large depth scale, as well as to distinguish the difference in the electronic properties at the very surface/interface and deeper into the bulk. The work function of LCP–LCPO was determined from the secondary electron cut-off measured at normal emission geometry, with sample BIAS voltage −9.2 V and using photon energy $h\nu$=47 eV and $h\nu$=1486.7 eV. The background of the SPES spectra was subtracted using a Shirley-type function; the photoelectron peak positions and areas were obtained by a weighted least-squares fitting of model curves (70% Gaussian, 30% Lorentzian) to the experimental data. The fitting of the P2p photoelectron spectra was performed taking into account the spin-orbit splitting of Δ(P2p$_{3/2}$- P2p$_{1/2}$) = 0.84 eV.

DFT calculations. DFT calculations were performed using the plane-wave- pseudopotential implementation of DFT contained in the Quantum-ESPRESSO suite of codes.[30] The exchange-correlation functional was constructed within a generalised-gradient approximation (according to the pbesol parameterisation.[31] Pseudopotentials were chosen of the ultrasoft type and required plane-wave energy cut-offs of 80 and 800 Ry for the wave functions and charge-density respectively. The BZ was sampled with 2×4×4 and 4×2×2 k-point grids for LCP and LCPO, respectively. In order to overcome the well-known problem of the

3

residual self-interaction afflicting approximate xc functionals and causing an over-delocalisation of d electrons we used a Hubbard correction to the standard DFT KS Hamiltonian (see, Refs.[32] for a non-exhaustive literature sample), according to the popular DFT+U approach. The effective on-site electronic interaction parameters were computed self-consistently employing a recently developed density-functional perturbation theory - based implementation of linear-response theory.[33]

The ab initio modelling of the LCP-LCPO system was focused on assessing the electronic structure of these materials and some aspects of their electrochemical behaviour. Calculations were aimed, in particular, at studying the shift of the electronic energy spectrum (valence and conduction bands) and of the density of states in dependence of Li content, for a comparison with the results of the experiments and at evaluating the average voltage of the two main phases (to verify the higher potential of LCPO). Table 1 compares the occupation of Co d states of LCP in three compositions at $x = 0$, $x = 0.5$ and $x = 1$ and reports the average voltage of the system (across the whole range of Li content) as obtained with DFT and DFT+U. While DFT predicts an average voltage of about 3.47 V for this system, the Hubbard corrected DFT+U result, 4.82 V, is in excellent agreement with experimental measurements (~4.8 V). In addition, DFT+U predicts for $Li_{0.5}CoPO_4$ a mixed-valence ground state with half of the Co ions in a 2+ state and half in a 3+ state, as expected from chemical intuition. DFT, on the contrary, predicts $Li_{0.5}CoPO_4$ to feature an average oxidation

state with valence electrons almost equally distributed among the Co ions. These results are qualitatively similar to those obtained for the Mn and Fe olivine phosphates, analogue to LCP.[34] Analogous information is collected for LCPO (Table 1). Only the $x = 1$ and $x = 0.75$ compositions are considered in this case (Figure 1). As for LCP, approximate DFT functionals fail to predict the oxidation of one Co to the 3+ state upon Li removal and achieve, instead, a "fake" metallic ground state where all the Co atoms are partially (although differently) ionized. When the Hubbard correction is used, instead, only one of the Co atoms switches to a 3+ oxidation state while all the others remain 2+. Note that the DFT+U re-establishes a strict numerical consistency between the occupations of the d states of Co atoms in the same
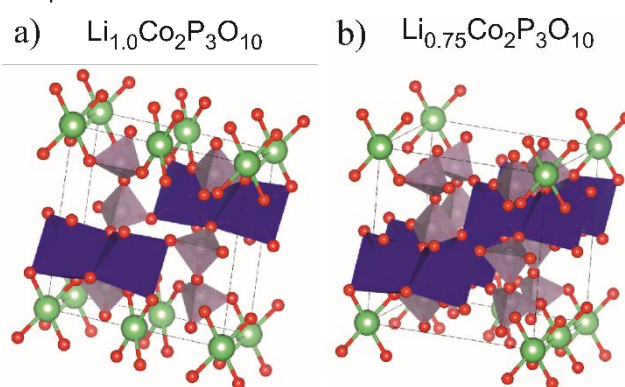
a) $Li_{1.0}Co_2P_3O_{10}$ b) $Li_{0.75}Co_2P_3O_{10}$

Figure 1 a, b) The simulation cell of $LiCo_2P_3O_{10}$ and $Li_{0.75}Co_2P_3O_{10}$ with three PO_4^{3-} polyanions building an oxy-anion group $P_3O_{10}^{5-}$: O, Li, P and Co are red, green, grey and blue, respectively.

Table 1. The total occupation of Co 3d states in Li_xCoPO_4 and $Li_xCo_2P_3O_{10}$. Average voltage V computed with DFT and DFT+U as compared to the experiment.

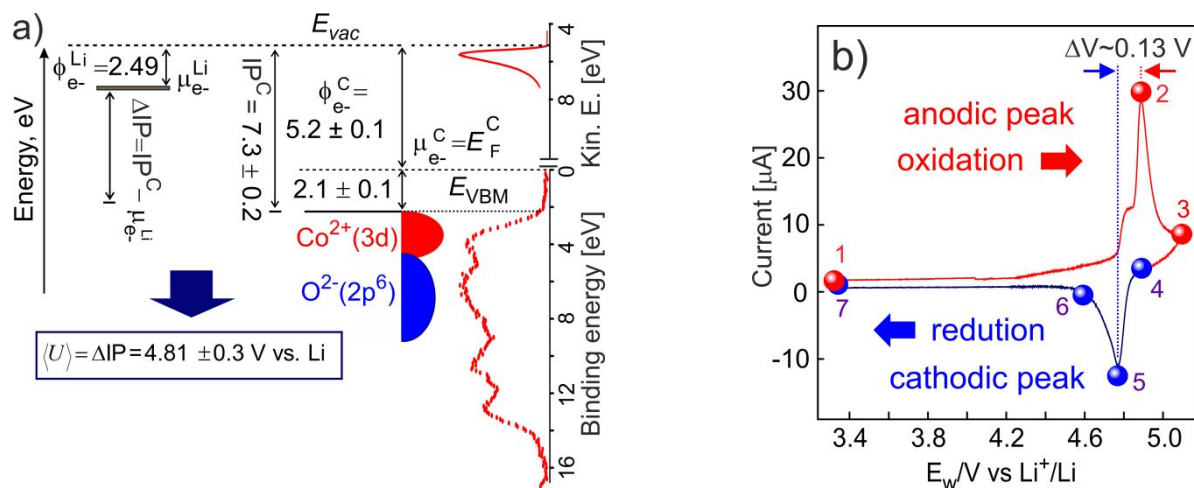|	$LiCoPO_4$	$Li_{0.5}CoPO_4$		$CoPO_4$	Voltage (V)
Valence state	Co^{2+}	Co^{2+}	Co^{3+}	Co^{3+}	
DFT	7.35	7.17	7.16	7.06	3.47
DFT+U	7.18	7.17	6.82	6.81	4.82
Exp.					4.8
	$LiCo_2P_3O_{10}$	$Li_{0.75}Co_2P_3O_{10}$			Voltage (V)
Valence state	Co^{2+}	Co^{2+}		Co^{3+}	
DFT	7.30	7.21; 7.25; 7.26			2.64
DFT+U	7.17	7.17		6.78	5.07

Figure 2 a) The VB spectrum (red dots) and the secondary electron cut-off (red line) of the pristine LCP –LCPO measured at hν=1486.7 eV and hν=47 eV, respectively. "Kin. E" is kinetic energy of photoelectrons. The relevant electron level energy diagrams of LCP-LCPO and metallic lithium are shown. E_{VBM}, ϕ_{e-}^C, ϕ_{e-}^{Li}, E_{vac} =0 are the valence band maximum, the electron work function of the cathode and lithium, the vacuum level, respectively. μ_{e-}^{Li} =E_F^A and μ_{e-}^C= E_F^C are the Fermi levels of the anode (lithium) and the cathode, respectively. The average voltage $\langle U \rangle$ of the battery cell is defined as: $\Delta IP = IP^C - \mu_{e-}^{Li}$ = 4.81 ± 0.3 eV. IP^C is the ionization potential of LCP−LCPO. For metals, the ionization potential equals to the work function: μ_{e-}^{Li} = IP^{Li}. b) The cyclic voltammogram of the LCP−LCPO cathode material cycled in the 1 M LiPF$_6$ in 4:1 wt/wt DMC:FEC with TMB (0.2% wt) electrolyte. ΔV is polarization potential. The colour balls show the potentials upon which the electronic properties and chemical composition were studied.

oxidation states, independently from the material of choice (phosphate or orthophosphate) and Li content. This is not true for approximate DFT functionals. Concerning the energetics, while DFT+U predicts the delithiation of the orthophosphate to be energetically more demanding than the phosphate (5.1 V vs 4.8 V), thus confirming the latter as the only electrochemically active phase in the system, the opposite is true for approximate DFT.

Calculation Details on XANES. The Co $L_{3,2}$- and Co $M_{3,2}$-edges of pristine LCP−LCPO are calculated by using CTM4XAS 5.5 program.[35] The Co^{2+} with high spin (HS) in O_h coordination geometry to np^63d^6 ground and np^53d^7 final states. Here, the principal quantum number n equals to n=2 and n=3 for the Co2p-Co3d transition and the Co3p-Co3d transition, respectively. The crystal field strength is $10Dq$ =1.05 eV for Co^{2+} (HS),[36] whereas $10Dq$ = 0.5 eV is used for Co^{3+} with HS state.[37] The influence of the charge transfer effects on Co $L_{3,2}$- and Co $M_{3,2}$- XANES was considering by using: a) the multiplet-averaged Coulomb interaction U_{d-d} =6.8 eV, b) the charge transfer energy Δ=1.0 eV from ligand p to transition metal d, and (c) the p-d transfer integral pdσ = −2.0 eV.[38]

RESULTS AND DISCUSSION

Evolution of occupied electronic states upon charging/discharging potential. The average voltage U of the cathode material vs. lithium is evaluated as the binding energy (per unit charge) of Li atoms in the bulk of fully delithiated ($x_1 = 0$) material to form the fully lithiated (x_2=1) compound:

$$\langle U \rangle_{x1,x2} = -\frac{E(Li_{x2}MX) - E(Li_{x1}MX) - (x_2 - x_1)E(Li_{bulk})}{(x_2 - x_1)e}$$

where e indicates the electronic charge; M= Co, X=PO$_4$ and M=Co$_2$, X=P$_3$O$_{10}$ for LCP and LCPO, respectively. The average voltage is often described as the difference in electrochemical potentials of the anode (μ_{e-}^A) and the cathode (μ_{e-}^C) (Figure S1,b) by considering the dominating electronic contribution to chemical potential of lithium.[39-41] By using density functional theory (DFT) within the Hubbard-corrected (DFT+U) functional (see the Experimental Section for details), the estimated average voltage of the olivine LCP is 4.82 V (Table 1). This value agrees excellently with the redox potential determined from photoemission experiments (Figure 2a) and electrochemical measurements (Figure 2b), thereby supporting the dominating role of the electronic factor to the battery voltage. The electronic structure of fully lithiated both LCP and LCPO is composed of Co^{2+} ($t^3_{2g}\uparrow t^2_{2g}\downarrow e^2_g\uparrow$) ions. For lithium
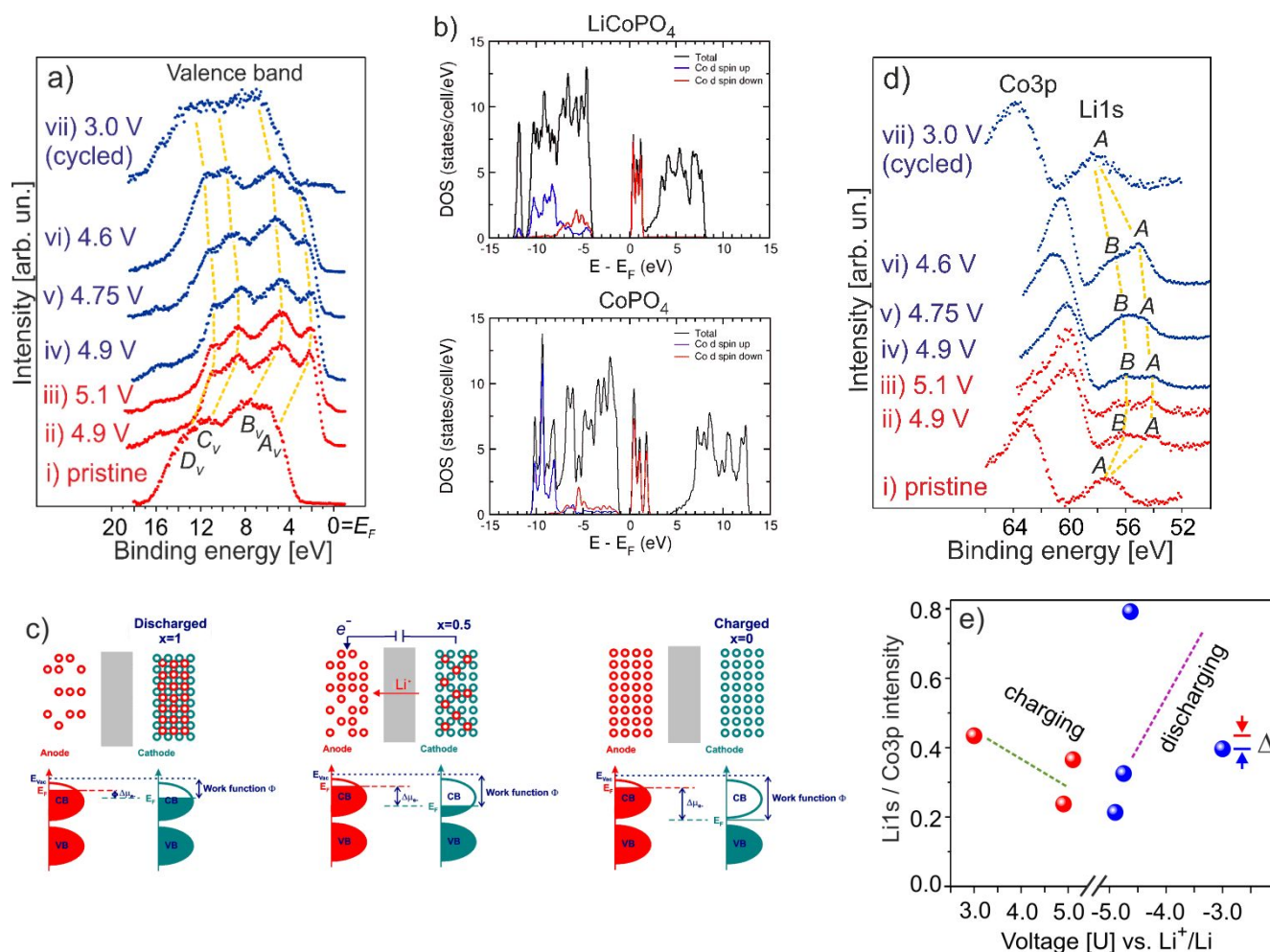
5

Figure 3 Evolution of the electronic states via electrochemical charging/discharging of LCP-LCPO. a) VB structure (charged- and discharged- states are shown in red and blue, respectively). b) The density of occupied and unoccupied electronic states of LiCoPO$_4$ (top) and CoPO$_4$ (bottom) near E_F calculated by using the DFT + U approximation. c) An illustration of the electrochemical potential shift of the cathode (E_F gray) with lithium content x (adapted from Ref.[48]). E_F, VB, CB, E_{vac} are the Fermi level, conductive band, vacuum level, respectively. A highest battery voltage is achieved for fully delithiated cathode. d) Li 1s- and Co 3p- core levels spectra: (i) pristine (after storing in a glove-box); charged state (ii, iii) and discharged state (iv-vii). The gradual shift of the spectral features towards (away) E_F upon delithiation (lithiation) is illustrated by the yellow dashed lines. e) The Li 1s and Co 3p photoemissions normalized to the Co 3p maximum intensity. Δ denotes the difference in the intensity ratio before and after the 1st electrochemical cycle. Probing depth of the photoelectron spectra is 70–80 Å.

content x=0.5 (Li$_{0.5}$CoPO$_4$), the DFT+U approximation predicts a mixed- valence ground state with half of the Co ions in a 2+ state and half in a 3+ state (Table 1). Our calculations show that the LCPO phase has a higher redox potential of 5.1 V (Table 1), which means that delithiation of the orthophosphate is energetically more demanding as compared to the olivine structure. Thus, LCPO is not involved in the electrochemical process at the given experimental conditions. The conclusion is also supported by the CV curves (Figure 2b) whose behavior is inherent to olivine-LCP.

The evolution of the valence band (VB) structure of LCP–LCPO experimentally measured at different charging/ discharging states is shown in Figure 3a. The four spectral features (A_v, B_v, C_v, D_v) are inherent for phosphates.[42] The A_v is associated with the t$_{2g}$ and e$_g$ states of Co; the B_v is ascribed to the Co 3d hybridized with O 2p bonding and antibonding states, whereas the C_v and D_v are related to the oxygen and phosphor strongly bound states.[25,43] Upon charging the battery cell, Li$^+$ ion leaves the cathode accompanied by a valence electron to maintain the charge neutrality of the host. In turn, it leads to a shift of all the photoelectron spectra towards lower binding energies, E_{bin}, which is equivalent to the E_F shifting towards the occupied electronic states of the cathode (Figure 3a,ii-iii). Upon delithiation, the E_F pins first a nearest Co 3d state, which

6

Table 2 Evolution of the work function (ϕ_{LCP}), valence band maximum (E_F - E_{VBM}) measured with different photon energies corresponding to different probing depths, and the changes in the ionization potential (IP) and interfacial dipole ($\Delta\delta_{dip}$) under electrochemical charging/discharging of the LCP-LCPO cathode

	$\phi_{e^-}{}^{LCP}$ $\pm$ 0.1 [eV] hυ=47 eV	VBM [a,b] $\pm$ 0.1 [eV] hυ=1486.7 eV	VBM [b] $\pm$ 0.1 [eV] hυ=984 eV	VBM [b] $\pm$ 0.1 [eV] hυ=812 eV	IP [d] $\pm$ 0.2 [eV]	$\Delta\delta_{dip}$ [c] $\pm$ 0.2 [eV] hυ=984eV
Pristine	5.20	2.1	3.25	3.25	8.45 (8.45)	-
4.9 V charge	5.65	-	0.85	0.95	6.5 (6.60)	1.95
5.1 V charge	5.75	-	0.70	0.60	6.45 (6.35)	2.00
4.9 V disch.	5.85	-	0.75	0.75	6.6 (6.6)	1.85
4.75 V disch.	5.60	-	1.00	0.95	6.6 (6.65)	1.85
4.6 V disch.	5.45	-	1.15	1.25	6.6 (6.7)	1.85
3.0 V disch.	5.35	-	3.15	2.80	8.5 (8.15)	0.05

a) average value obtained on several samples.

b) VBM = [E_F - E_{VBM}] is determined by the linear extrapolation of the onset of the valence band emission to the baseline. The downward band bending (i.e. away from E_F at the surface) of the pristine LCP-LCPO impacts E_{VBM} and core levels energy position probed with different photon energies.

c) The existence of an interfacial dipole at the vacuum/pristine LCP-LCPO interface was not experimentally established.

d) Estimated as the sum of $\phi_{e^-}{}^{LCP}$ and VBM (hυ=984 eV); and VBM (hυ=812 eV) (in brackets).

e) $\Delta\delta_{dip}$= $\left|\Delta\phi_{e^-}{}^{LCP}\right|$ $-$ $\left|\Delta VBM\right|$.

results in Co^{2+} → Co^{3+} oxidation in accordance with the previous results on different LCP polymorphs.[44,45] At 5.1 V charging state, the E_F relative shift equals 2.7 $\pm$ 0.2 eV corresponding to the valence band maximum (E_F - E_{VBM}) of 0.6 $\pm$ 0.1 eV (Figure 3a,iii). The density of occupied and unoccupied states near the Fermi level (E_F) of LiCoPO$_4$ and CoPO$_4$ are illustrated in Figure 3b. As evident, the change of the Co^{2+} to Co^{3+} oxidation state upon delithiation lowers the energy of the empty d states (minority spin) reducing the gap in the Kohn-Sham energy spectrum of the material from 4 to 1 eV. Thus, the experimental results fully agree with the DFT+U calculations, which evidence a significant shift of E_F to the occupied electronic states for fully delithiated LCP (Figure 3b). The opposite energy shift of the occupied states is observed with lithium insertion to the cathode (Figure 3a,iv-vii). In this case, valence electrons are transferred to empty electronic states of the

cathode material resulting in a reduction of Co^{3+} to Co^{2+} (see the next section for details). The E_F - E_{VBM} approaches its initial (pristine) energy position at a discharging state of 3.0 V vs. Li$^+$/Li (Figure 3a,vii). Table 2 shows that the work function, $\phi_{e^-}{}^{LCP}$ increases (decreases) gradually upon delithiation (lithiation) of the cathode, which evidences the continuous change of the E_F with respect to the E_{VBM}. An important issue of the electrode/electrolyte interface is the electrical double layer formation, which might impact the battery performance. Generally, the presence of the interfacial dipole, δ_{dip}, induced by the electrolyte contact and/or electrochemical reactions, can be estimated from the relative change of the $\phi_{e^-}{}^{LCP}$ and the E_F-E_{VBM}.[46,47] The valence band maximum is significantly more shifted than the $\phi_{e^-}{}^{LCP}$ upon charging LCP-LCPO, thereby evidencing the dipole formation at the cathode/electrolyte interface (Table 2). In
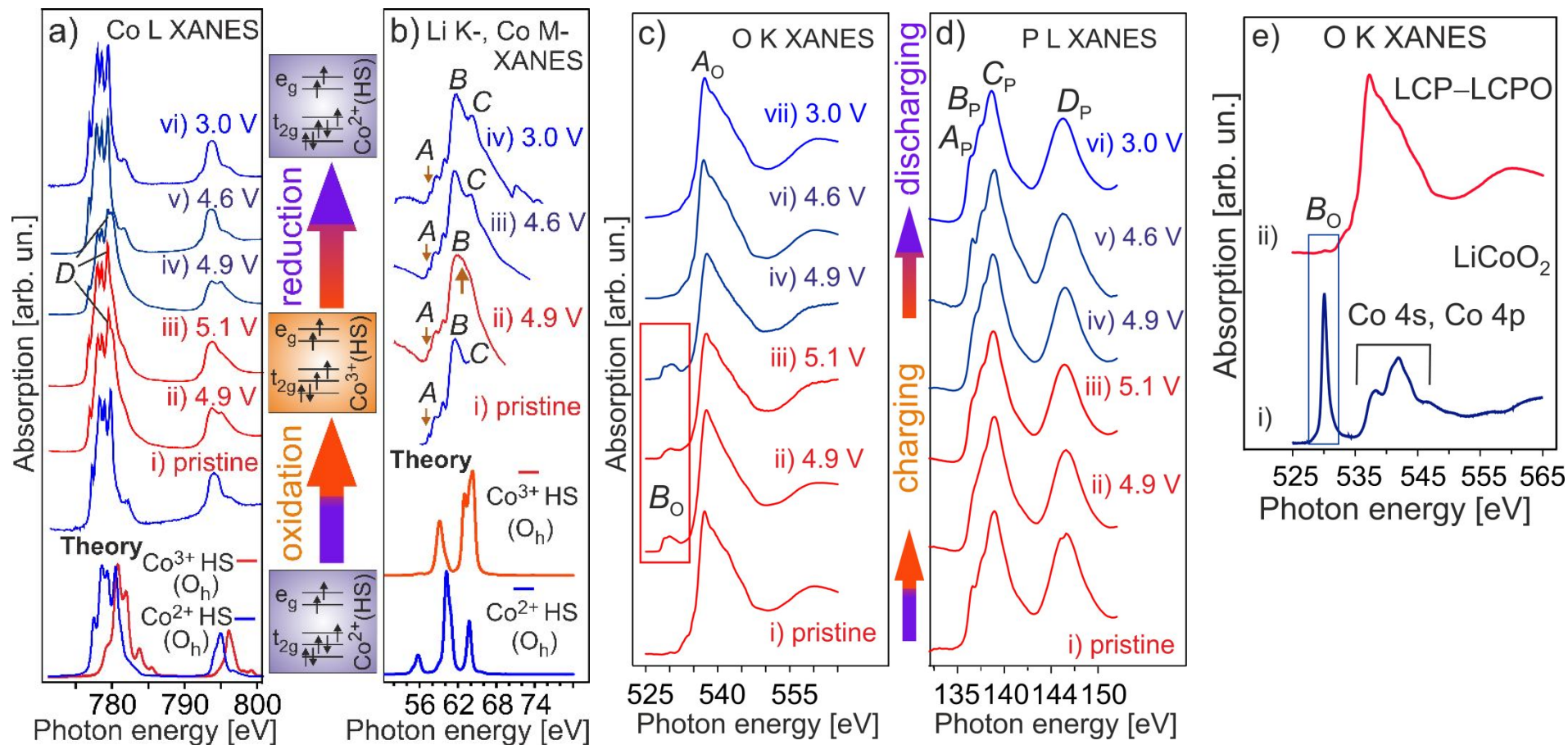
7

Figure 4 Evolution of a) Co $L_{3,2}$-, b) Li K- (*A* peak at 57.5 eV) and Co $M_{3,2}$-, c) O K-, d) P L- XANES via electrochemical charging/discharging of the LCP-LCPO cathode: (i) pristine (after storing in a glove-box); charged states and discharged states are shown in red and blue, respectively. The high energy shoulder of the Co $M_{3,2}$ - edge is denoted by the pointing-up arrow (ii). Theoretical calculations of the Co $L_{3,2}$ - (a) and Co $M_{3,2}$ - (b) edges are shown at the bottom. The evolution of the ground state electronic configuration at the Co-site upon oxidation and reduction of Co-ions is shown between panels a) and b). e) The O K- XANES of $LiCoO_2$ layered structure oxide (i) and LCP–LCPO (ii).

1
2
3
4
5
6
7
8
9
10
11
12
13
14
15
16
17
18
19
20
21
22
23
24
25
26
27
28
29
30
31
32
33
34
35
36
37
38
39
40
41
42
43
44
45
46
47
48
49
50
51
52
53
54
55
56
57
58
59
60

fact, the opposite direction of the interfacial dipole with respect to the E_F shift reduces the $\phi_{e^-}^{LCP}$ value. The maximal magnitude of $\Delta\delta_{dip}$=2.0 eV is achieved at 5.1 V charging potential and it gradually decreases again upon discharging the battery cell, fully disappearing at the 3.0 V (Table 2). In spite of a certain degree of uncertainty about the IP value (due to the dipole layer contribution to the experimentally determined $\phi_{e^-}^{LCP}$),[41] there is a clear trend in the decrease (increase) of the ionization potential upon delithiation (lithiation) of the cathode. The observed E_F shift is caused by purely electronic effects, which is different from chemical shift promoted by interfacial chemical reactions. An illustration of the electrochemical potential shift upon de/lithiation of a cathode material, assuming the validity of a rigid band model, is shown in Figure 3c.

Due to the electronic nature, all core-levels have to be shifted upon charging/discharging of the cathode in a similar manner to the VB structure. The evolution of the Li 1s and Co 3p photoemission spectra during 1st electrochemical cycle is shown in Figure 3d. The decrease (increase) of the lithium content upon charging (discharging) of the cathode material is well visible as a change of the Li 1s photoelectron intensity and the Li 1s to Co 3p ratio intensity (Figure 3d and 3e, respectively). Intensity of the spectral feature A associated with the lattice lithium is decreased upon charging of LCP-LCPO, whereas the second feature B becomes well resolved (Figure 3d). Note also that the A spectral component does not completely disappear at 5.1 V charging state. Upon lithiation of the cathode the B intensity is hidden again by superposition with the A peak, coming from the increase of Li content in the host. The component B can be ascribed to both, due to side reactions at the CEI and Li$^+$ ions hosted in the LCPO phase. The first suggestion is supported by the A and B energy difference of ~2 eV characteristic for the LiPF$_6$ salt and its decomposition product Li$_x$PO$_y$F$_z$.[49] On other hand, our DFT calculations show that Co^{2+} of LCPO has a slightly higher oxidation potential compared to LCP (see Table 1), which also means that a part of the lithium ions could remain in the LCPO lattice upon the current experimental conditions. An incomplete electrochemical delithiation in conventional olivine LiCoPO$_4$ being charged to 5.3 V vs. Li$^+$/Li was earlier reported.[50] The effect was assigned to severe electrolyte oxidation above 4.8 V leading to a redox gradient between the surface and bulk of the cathode. The electrolyte degradation usually comes with the involvement of the lattice lithium into chemical reactions at the CEI, which would lead to irreversible Li$^+$ loss. In our case, only a slight drop (Δ) of the Li 1s intensity is observed after the 1st cycle (Figure 3e), mostly assigned to loss of lithium contributing to the CEI formation. Thus, the lattice lithium content does not change significantly, evidencing that the cathode/electrolyte interface remains Li ion conducting.

Evolution of unoccupied electronic states upon charging/discharging potential. Li$^+$ release upon charging potential, accompanied by the removal of a valence electron, would lead to an electronic hole formation, which can be probed by XANES measurements (Figure 4a–d). The Co L$_{3,2}$- and Co M$_{3,2}$-edges are dominated by the electron transition to the unoccupied Co 3d, 4s states from the Co 2p- and Co 3p- core levels, respectively.[36] The Co L$_{3,2}$- edge of the LCP–LCPO pristine cathode material exhibits spectral features consistent with Co^{2+} (t$^3_{2g}$↑t$^2_{2g}$↓e^2_g↑) ions in the high spin (HS) state and in octahedral (O$_h$) coordination with oxygen. The energy positions of the Co L$_{3,2}$- and Co M$_{3,2}$- edges at ~779 eV (Co L$_3$) and 62 eV, respectively, agree well with atomic multiplet calculations (Figure 4a,b) and the experimental research.[43,51] In the case of the Co M$_{3,2}$- edge (Figure 4b), the empty Co 3d and Co 4s states are strongly overlapped with empty Li 2p orbital due to the energy vicinity of the Li 1s and Co 3p core levels. The Co^{2+} to Co^{3+} oxidation upon charging of LCP-LCPO is evidenced as a rise in intensity of the high energy shoulders of the Co L- edge (D feature at ~780 eV) and Co M- edge (an up arrow at ~63 eV) (Figure 4a and 4b,ii). Upon discharging the cathode, the spectral features (D and B in Figure 4a,v,vi and 4b,iii, respectively) decrease in intensity becoming similar to that of the pristine LCP–LCPO, thereby evidencing the Co^{3+} → Co^{2+} reduction. We have also observed that the intensity of the high energy shoulder D (Figure 4a) varies for different areas of LCP–LCPO (Figure S2), indicating that only a part of Co^{2+} ions are oxidized to Co^{3+}. As it was already mentioned, the reason can be assigned to the presence of Co^{2+} ions in LCPO, which is not electrochemically active at the current experimental conditions. On the other hand, inhomogeneous distribution of the LCP and LCPO phases across the sample, as well as leaching of MoO$_3$ from the surface (see discussion below) could lead to insulated areas resulting in a loss of electronic conductivity between some parts of active material. In principle, such a phenomenon as self-discharge of the cathode would lead to the Co^{3+} → Co^{2+} reduction via electron transfer to the Co 3d site. However, this electron transfer would also lead to a shift of all occupied states away from E_F, whereas our results show a clear shift of the occupied states to the E_F upon charging (i.e. upon delithiation) of the LCP-LCPO cathode (Figs. 3a, 3d, S3,

9

S4). Therefore, we suggest that self-discharge is not the main reason of the presence of Co^{2+} ions in delithated cathode.

Whilst the Co $L_{3,2}$- and Co $M_{3,2}$- edges evidence the involvement of cobalt in the redox reaction, the O K- and P $L_{3,2}$-XANES give insight into the stability of PO_4 polyanion at high voltage. The evolution of the O K- and P $L_{3,2}$ - edges of LCP–LCPO vs. charging/discharging is shown in Figure 4c,d. The O K- edge of the pristine LCP–LCPO (Figure 4c) is typical for orthophosphate (PO_4) compounds.[51-54] The main feature A_O at 537.3 eV is due to the electron transition from the O 1s core level to the empty O 2p orbital. In 3d transition metal (M) oxides, like $LiMO_2$, the O2p state is hybridized with the 3d- state and the 4sp- state of the metals. These states are observed at a lower energy and a higher energy, respectively, from the main feature.[55] The O K- edge of phosphates is commonly broader due to the presence of phosphorous states

(in addition to the metal states, see Figures 4e, S5, Ref.[56]), which form a strong covalent oxygen-phosphor bonding in the PO_4 unit. Upon charging the cathode, a new spectral feature (B_O ~530 eV) appears in the O K- edge (Figure 4c). We do not assign the B_O feature with the involvement of oxygen in charge compensation (i.e. with the $O^{2-} \rightarrow O^-$ oxidation), because the O 2p band is energetically situated far away from the E_F (Figures 2a, 3a). By other words, the O 2p band is not pinned by the E_F even at 5.1 V charging potential. Upon discharging LCP–LCPO, the feature B_O vanishes (Figure 4c,iv-vii) and the O K- edge recovers for the spectral features of the pristine cathode material (Figure 4c). Thus, the reversible changes in the B_O intensity of the O K- edge are assigned to an increasing number of unoccupied Co 3d–O 2p hybridized states upon delithiation, as well as changes in the Co 3d-O 2p hybridization, similar to that observed for $LiFePO_4$.[57,58]
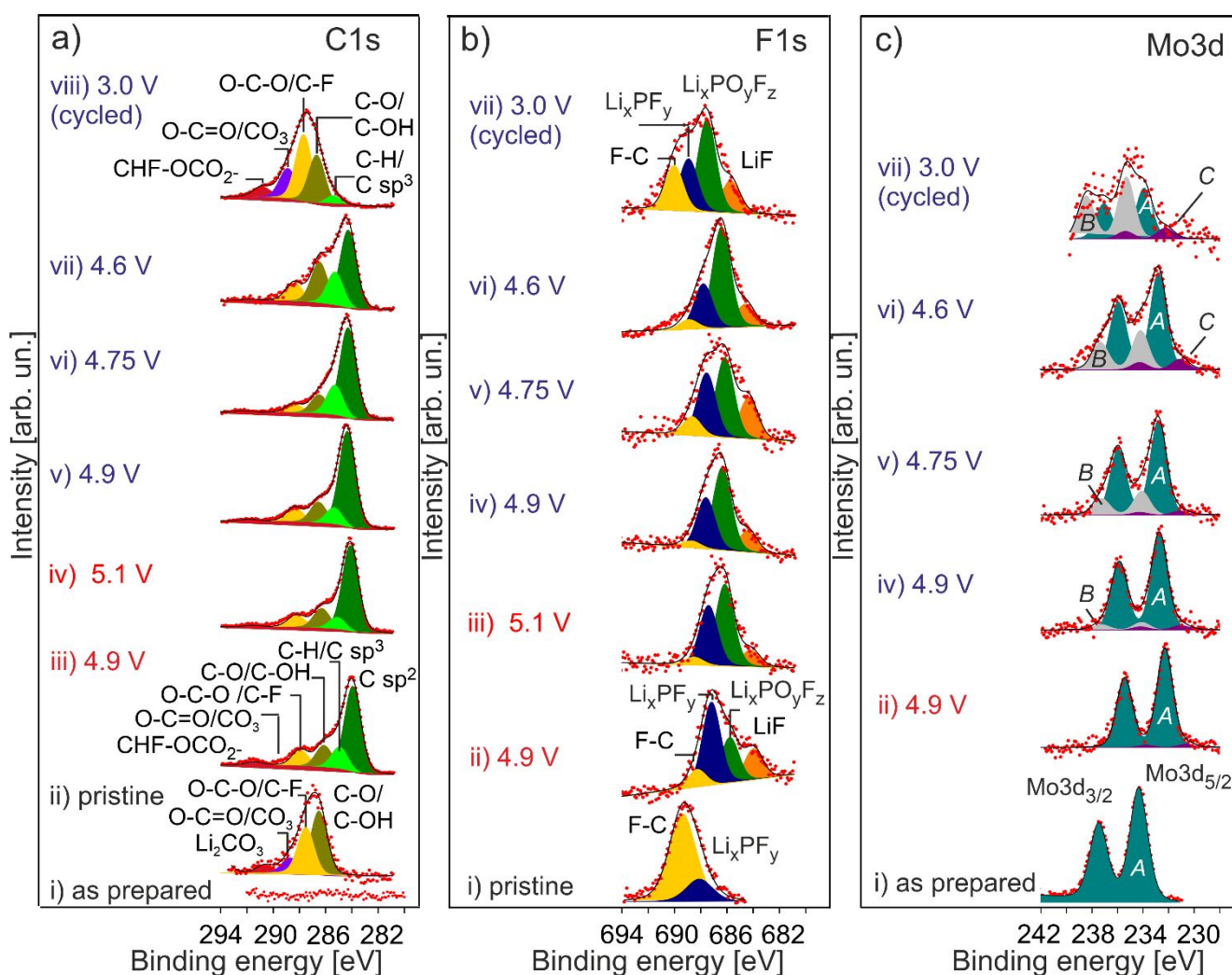

Figure 5 Evolution of a) the C 1s- (hν=1041 eV), b) F 1s- (hν=1457 eV) and c) Mo 3d- (hν=984 eV) photoemission spectra upon charging/discharging of LCP–LCPO. Probing depth d~70 Å. As prepared cathode (a, c) was measured at hν=1487.7 eV. Pristine (after storing in a glove-box) (b, i). Charged states and discharged states are shown in red and blue, respectively. c) The Mo^{6+} oxidation state is denoted as A (c). The occurrence of spectral feature (B) is manifested as a rise of the shoulder between the Mo $3d_{5/2}$ and Mo $3d_{3/2}$ photoemissions (c, iii-vi). The reduced Mo^{5+} state is denoted as C. All spectra are normalized to their maximum intensity.

10

The P $L_{3,2}$- edge exhibits A_P (136.7 eV) and B_P (137.8 eV) spectral features associated with the electron transition from P $2p_{3/2}$ and P $2p_{1/2}$ core-levels to the first empty 3s antibonding state. The C_P component at 138.9 eV is related to the transition to the empty 3p orbital. Although the $2p \rightarrow 3p$ transition is dipole forbidden, it can be favourable due to the mixing of P 3p orbital with oxygen and metal states.[59,60] The next peak D_p at the energy of ~146 eV is generally assigned to a $2p \rightarrow 3d$ transition (so called "shape resonance").[60] Figure 4d demonstrates that the initially well-resolved A_P and B_P features are smoothed upon delithiation, but become well resolved again after lithiation of LCP–LCPO, which evidences the reversible electronic configuration at the phosphorous site. In phosphates, a Li ion forms a fully hybridized band with the polyanion, where the P–O bond is strongly covalent. Therefore, the removal of Li^+ would lead to the redistribution of the electronic density between phosphorus and oxygen, resulting in a change of the polarization in the Li–O–P bonding.[42,61] Any variations in the electronic density around the oxygen site would also involve the empty 3p and 3s phosphorus states, as it is observed in P $L_{3,2}$ edge (Figure 4d). Thus, the correlated evolution of A_P and B_P features of the P $L_{3,2}$- edge (Figure 4d) and of B_O pre-edge peak of the O K- edge (Figure 4c) evidences an altering of the polarization between lithium and the polyanion, which is reversible upon de/lithiation of LCP–LCPO.

Evolution of chemical composition of the CEI upon electrochemical cycling. An advantage of electrolytes composed of fluorinated components is their capability to support a high voltage (> 5.0 V) via the formation of a stable CEI.[62] The fluorinated ethylene carbonate (FEC) suppresses the decomposition of $LiPF_6$,[63] facilitates the charge transfer and decreases the resistance at the interface.[64] Therefore, the evolution of the F1s- and C1s- photoemission spectra vs. a charging/discharging state can give insight into the interfacial chemical composition and, accordingly, the interface stability at high voltage potential.

The C 1s photoemission spectra measured from ≥ 4.9 V (charging state) to the 3.0 V (discharging state) are shown in Figure 5a. The most intense peak with E_{bin} = 284.1 ± 0.2 eV (Figure 5a,iii-vii) is inherent to the C-C bond of graphite-like structures,[63] having predominately sp^2 type bonding. The spectral feature at E_{bin} =285 ± 0.3 eV is ascribed to sp^3 bond and hydrocarbons (C–H bond).[65] Note that polyvinylidenfluoride (PVDF), as an indispensable component of composite cathode materials, contributes to the C

1s photoelectron spectra in a similar energy range.[66] In our case, neither conductive carbon nor PVDF are used in LCP–LCPO. Thus, only the organic (solvent) components of the electrolyte and its degradation products are involved in the CEI formation. The spectral features at higher binding energies (Figure 5a) are ascribed to C-O (286.3 ± 0.3 eV),[27,67] C-F/ O-C-O/ C=O and/or polar carbonate (R-CO_3) (288.0 ± 0.3 eV),[64,68-70] Li_2CO_3 (~290 eV).[27,64,70] The weak feature at 291.3 eV can be ascribed to CH_2-CF_2,[71] –CHF-OCO_2,[69] or poly(CO_3),[70] as the result of the FEC decomposition. No significant changes in the shape of the C 1s photoemission spectra until 4.75 V discharging state (Figure 5a,iii-vi) evidence a high stability of the CEI at high potential. Below 4.75 V discharging state, the spectral features associated mostly with carbon-fluorine and carbon-oxygen bonds rise in intensity as compared to the C-C and C-H related species (Figure 5a,vii). For the electrochemically cycled LCP–LCPO, the spectral feature associated with the sp^2 bond vanishes in the C 1s photoemission (Figure 5a, viii); the latter becomes very similar to that after storing the pristine sample in a glove-box (Figure 5a, viii, Figure S6,a).

The fluorine-related species contributing to the CEI formation at high charging/discharging potential are mostly $Li_xP_yF_z$, $Li_xPO_yF_z$, LiF and C–F due to decomposition reactions of both the inorganic Li salt and organic FEC. The F 1s photoemission at 687.1 ± 0.3 eV is assigned to Li_xPF_y (Figure 5b,ii-vi), whereas LiF is situated at lower energy (E_{bin}=684.4 ± 0.3 eV) in agreement with the 3.0 ± 0.5 eV difference between these two chemical species.[68-72] Note that the interpretation of the F1s components in the energy range between the Li-F and Li-P-F species is still debated (see for example Refs.[68-71,73]). In both the composite cathode- and anode- materials, the F1s photoemission in the range of 685.8 eV ± 0.6 eV is often ascribed to C-F bond,[68,69,71] or to Li-P-O-F species of $Li_xPO_yF_z$.[70,73,74] In the second case, the C-F bond is displaced at higher energies from $Li_xPO_yF_z$ and Li_xPF_y. We attribute the F1s peak at 686.0 ± 0.3 eV to Li-P-O-F, since the P2p photoemission shows a similar trend in the change of the Li_xPF_y to $Li_xPO_yF_z$ intensity ratio vs. charging/discharging potential (Figure S3). Accordingly, the spectral feature at 688.7 ± 0.4 eV is ascribed to the C-F species whose amount is markedly increased after the 1st electrochemical cycle (Figure 5b).

The F 1s- and C 1s- photoemission intensities demonstrate the competitive trend upon de/lithiation of the LCP–LCPO cathode (Figure S7a,b), which gives us the suggestion that the CEI becomes more organic and more inorganic upon delithiation and lithiation, respectively. A dynamic behaviour in composition and thickness of

11

solid-electrolyte interface, via the formation of an organic-like layer with lithiation and becoming more inorganic with delithiation, was earlier reported for a silicon anode.[75] Besides the pointed organic/inorganic composition switching, our depth-resolved experiments revealed a gradient concentration of inorganic components with their depletion at the core CEI and a higher content close to the CEI surface (Figure S8).

The Mo3d photoemission spectra vs. charging/discharging potential are shown in Figure 5c. As prepared, molybdenum exhibits Mo^{6+} oxidation state at E_{bin} [Mo $3d_{5/2}$] =234. 3 eV, which evidences the MoO_3 formation on the LCP–LCPO surface (Figure 5c,i). It worth to note that in X-ray diffraction no crystalline phase of MoO_3 is observed (Figure S9) despite the rather high annealing temperature (see the experimental section). As MoO_3 is clearly found by the surface sensitive SPES/XPS techniques, the assumption of a thin nanocrystalline layer of MoO_3 is consistent with the experimental findings. Upon charging (discharging) the cathode, the whole Mo 3d photoemission is shifted to lower (higher) binding energies (Figure 5c), which is attributed to the electrochemical potential shift observed for all photoemission spectra of LCP–LCPO (see also Figures S3, S4). In contrast to LCP–LCPO, the MoO_3 layer undergoes irreversible changes in chemical composition manifested as the occurrence of additional states (B, C) at higher- and lower- binding energies from the Mo 3d photoemission (Figure 5c). These changes become more pronounced with time of electrochemical cycling (Figure 5c,iii-vi). The chemical state denoted as B can be assigned to the surface reconstruction induced by chemical reaction of MoO_3 and the electrolyte. Although Mo (VI) is the highest oxidation state of molybdenum, the binding energy of Mo^{6+} can vary in a large energy range. For example, h-MoO_3 nanostructure of pyramidal phase exhibits Mo $3d_{5/2}$ =235.4 eV, which is more than a half eV higher as compared to hexagonal nanoplates.[76] Fluorination of transition metal oxides would also lead to higher E_{bin} due to the more electronegative F^- ion.[77] The spectral feature C (Figure 5c,v,vi) is ascribed to reduction of Mo (VI) to Mo (V) according to ~1.6 eV energy difference between the two chemical states.[78] Note that the possible impact of X-ray radiation on reduction of MoO_3,[79] is found to be negligible, whereas the trend in reduction of Mo (VI) to Mo (V) with exposure time of the cathode to electrolyte is obvious (see Figure S10). Synergisms of the Mo 3d- and F 1s-, and C 1s- photoelectron spectra (Figure 5) suggests that MoO_3 and the FEC molecule (Figure S11) are linked to chemical reactions at the cathode/electrolyte interface. A significant

depletion of the coating after the 1st electrochemical cycle, evidenced as a decrease of the Mo3d intensity (Figure S7,c), is ascribed to molybdenum dissolution from the surface. The observed changes of the Mo 3d photoemission spectra can be assigned to the involvement of MoO_3 into catalytic reactions with the decomposition products of the electrolyte. This oxide is well known to be a catalyst for selective oxidation of a wide range of organic compounds, such as cycloalkanes (C_nH_{2n}),[80] methane (CH_4),[81] methanol,[82] etc., where the reactions are often accompanied with reduction of Mo (see for example Ref.[83]), and the formation of volatile molybdenum compounds during catalysis in liquid phases.[84] Oxidation of hydrocarbons at the MoO_x/LCP–LCPO surface could explain their significant decrease at the CEI layer of the electrochemically cycled cathode (Figure 5a,vii). Note, although the abovementioned catalytic conversion of organic compounds is favourable at elevated temperatures or/and higher pressure, the thermodynamic limit for the reactions might be shifted to lower temperatures taking into account a small and enclosed space for the reactions in the battery cell. As an example, in recent experiments the internal pressure increase in a $LiCoO_2$ (LCO) cell was attributed to the evolution of gaseous decomposition products whose amount increases proportionally to the cell voltage and the time for the battery charge.[85] Regarding electrolyte oxidation, various oxidation pathways of organic solvents and the $LiPF_6$ salt were proposed in the past (see Refs.[16,85-88]). The oxidation at high voltage can be triggered by highly reactive single oxygen ($^1O_2$),[16,85] presence of H_2O, and protons. It is noteworthy that the formation of $^1O_2$ is coupled to a release of oxygen from the transition metal oxide lattice,[16,86] which is obviously not the case for LCP–LCPO since irreversible changes in the electronic structure are not observed after the electrochemical cycle. However, a correlation between the electrolyte oxidation and the reduction of Mo (VI) (Figure 5a-c) can be a sign of electronic hole transfer from the Mo 4d valence state to the electrolyte. Another possible reaction pathway for the reduction $Mo^{6+} \rightarrow Mo^{5+}$ is hydrogen intercalation into MoO_3 according to the chemical reaction: $MoO_3 \xrightarrow{H} H_xMoO_3 \rightarrow MoO_2 + 1/2\ H_2O$.[89] Hydrogen atoms could be formed by dissociation of H_2 on the MoO_3 surface taking into account the catalytic properties of the oxide,[89] or via reduction of H^+ to H_2 on the negative electrode followed by migration of the reaction products across the separator, as pointed out in Ref.[85] It is well known that proton or water, as trace moisture in the electrolyte, dissociate the PF_6^- anion to HF and highly reactive PF_5; this reaction takes place
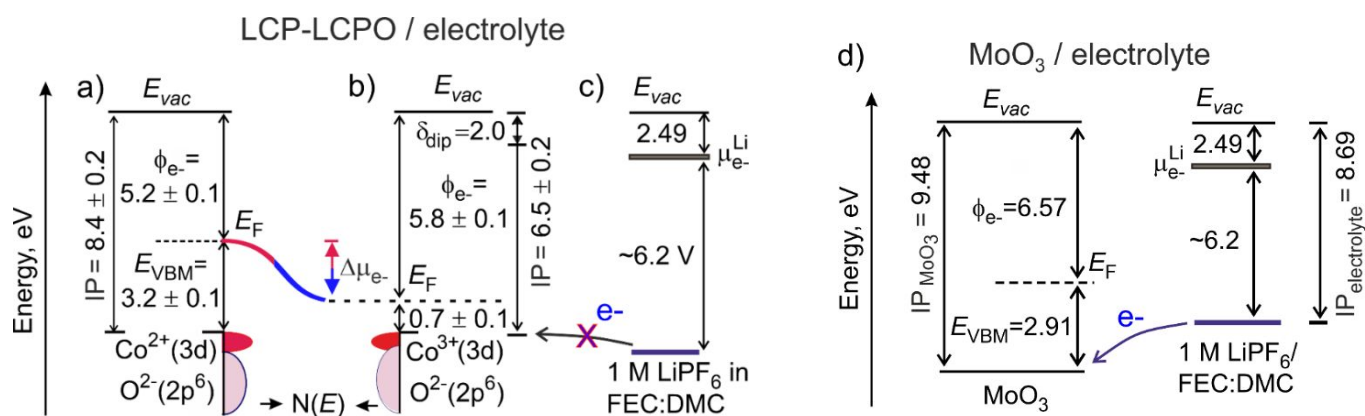
Figure 6 The electronic levels of a LCP−LCPO cathode: a) pristine and b) charged to 5.1 V vs. Li+/Li. E_{VBM} (hν=984 eV, probing depth ~80 Å), IP, E_F, ϕ_{e-}, δ_{dip} are the valence band maximum, ionization potential, the Fermi level, work function, interfacial dipole, respectively. $\Delta\mu_{e-}$ is the electrochemical potential difference between the pristine and charged LCP-LCPO. c) The oxidation potential of the 1 M LiPF6 salt in FEC:DMC (1:4 wt%) on glassy carbon (Ref.[3]); μ_{e-}^{Li} is the electrochemical potential of metallic lithium. d) The electronic levels of MoO3 (adapted from Ref.[91]) and the electrolyte are shown for comparison. All levels are plotted with respect to the vacuum level, E_{vac}

already at room temperature.[86] At high voltage potential, highly acidic species (H+ or HF) promote further electrolyte oxidation.

Thus, the significant changes in chemical composition of the CEI − while the intrinsic electronic properties of LCP−LCPO are mostly reversible after the 1st electrochemical cycle − gives us a strong argument regarding a proton transfer reaction to the organic solvents,[87,88,90] or/and electronic hole transfer from the valence state of MoO6 to the electrolyte. The reasons of stability of LCP−LCPO against chemical reactions with the FEC containing electrolyte and instability of MoO3 become also clear from the analysis of the experimentally obtained energy level diagrams (Figure 6). The electron ionization potential for the pristine LCP−LCPO at the surface is IP= 8.4 ± 0.2 eV (Figure 6a) is higher as compared to the IP measured deeper to the bulk (see Figure 2a and Table 2). This difference is due to a downward band bending with a depth, resulting in a shift of the electronic levels away from E_F at the surface for the pristine LCP−LCPO. Delithiation of the cathode lowers E_F. However even at 5.1 V vs. Li+/Li (Figure 6b), E_F is still higher of the oxidation potential of the 1 M LiPF6 salt in FEC/DMC (6.2 V vs. lithium),[3] Figure 5c. It makes unfavorable electronic charge transfer between the electrolyte and LCP-LCPO. On the contrary, the energy diagram of MoO3/electrolyte interface evidences the high probability for electron transfer from the electrolyte oxidation level to the valence state of MoO3 (Figure 6d). Accordingly, such charge transfer will lead to the reduction of the oxide and the oxidation of the electrolyte.

CONCLUSIONS

This work represents a comprehensive study of the intrinsic stability of the LiCoPO4 -LiCo2P3O10 (LCP−LCPO) cathode material for 5 V Li ion batteries under electrochemical cycling of the battery cell to 5.1 V (vs. lithium). The model thin film cathode material does not contain conductive carbon, whereas electron transfer kinetics for redox process is very high in contrast to conventional LiCoPO4 olivine structure. Whilst LCP and LCPO are insulators, tailoring the olivine structure with the orthophosphate coupled to a MoO3 coating is the reason of improved electronic conductivity due to the strongly correlated nature of the system. The electronic properties and structure of LCP-LCPO are fully reversible after the 1st electrochemical cycle. The involvement of the lattice oxygen in oxidation is not observed even at 5.1 V. Instead, XANES experiments demonstrate reversible occupation of the Co 3d–O 2p hybridized empty states and change of their hybridization, as well as the variation of the polarization in the Li-O-P bond upon delithiation and lithiation. For the first time, an average voltage of ~5.1 V is confirmed for LiCo2P3O10 by using the DFT+U approximation.

The high stability of the LCP-LCPO cathode at high voltage potential is due to a sufficiently large energy gap between the electrochemical potential of the cathode and the oxidation level of 1M LiPF6 FEC/DMC, which makes electron transfer from the electrolyte to the cathode unfavorable. In contrast, MoO3 layer on the top of LCP-LCPO undergoes chemical reactions with the

electrolyte at charging the cathode to 5.1 V. It leads to a surface reconstruction of coating, the reduction of Mo(VI) and a gradual leaching of the oxide layer during electrochemical cycle. The possible pathways for the electrolyte oxidation contributing to the cathode-electrolyte interface formation are mostly assigned to: a) H^+ transfer reaction to organic solvents (DMC and FEC) and, b) electron transfer from the electrolyte to the valence states of MoO_3, as supported by the experimentally obtained energy diagrams. In addition, hydrogen intercalation into MoO_3 could be another reason of the oxide reduction. Taking into account that MoO_3 is catalytically active towards selective oxidation of hydrocarbons, as well as considering the volatility of reacted molybdenum compounds, this oxide is probably not the best protective layer against liquid electrolytes with carbon functional groups, at least for a long time electrochemical cycling. On the other hand, in order to enhance electronic conductivity of high voltage cathode materials, Mo-doping or MO_3 coating could be an advantage in case of solid electrolytes.

ASSOCIATED CONTENT

Supporting Information. The supporting information includes the plots of theoretical capacity and electrochemical potentials of various cathode materials. The Co L- and O K- edges XANES, evolution of the F1s-, P2p-, O1s- photoelectron spectra and of the F1s-, C1s-, Mo3d- intensities vs. charging/discharging potential, depth-resolved PES, dependence of the Mo(V)/Mo(VI) ratio vs time of X-ray beam exposure, survey XPS, XRD, cyclic voltammetry, SEM images and EDS maps.

Notes

The authors declare no competing financial interest.

REFERENCES

(1) Lu, Y.- C.; Gallant, B. M.; Kwabi, D. G.; Harding, J. R.; Mitchell, R. R.; Whittingham M. S.; Horn, Y. S. Lithium–Oxygen Batteries: Bridging Mechanistic Understanding and Battery Performance. *Energy Environ. Sci.* **2013**, *6*, 750-768.

(2) Cheng, X. B.; Huang, J.- Q.; Zhang, Q. Review - Li Metal Anode In Working Lithium-Sulfur Batteries. *J. Electrochem. Soc.* **2018**, *165*, A6058- A6072.

(3) Delp, S. A.; Borodin, O.; Olguin, M.; Eisner, C. G.; Allen, J. L.; Jow, T. R. Importance of Reduction and Oxidation Stability of High Voltage Electrolytes and Additives. *Electrochim. Acta* **2016**, *209*, 498-510.

(4) Richards, W. D.; Miara, L. J.; Wang, Y.; Kim, J. C.; Ceder, G. Interface Stability in Solid-State Batteries. *Chem. Mater.* **2016**, *28*, 266-273.

(5) Padhi, A. K.; Nanjundaswamy, K. S.; Goodenough, J. B. Phospho-olivines as Positive-Electrode Materials for Rechargeable Lithium Batteries. *J. Electrochem. Soc.* **1997**, *144*(4), 1188-1194.

(6) Xu, B.; Qian, D.; Wang, Z.; Meng, Y. S. Recent Progress in Cathode Materials Research for Advanced Lithium Ion Batteries. *Mater. Sci. Engineer. R* **2012**, *73*, 51-65.

(7) Metzger, M.; Sicklinger, J.; Haering, D.; Kavakli, C.; Stinner, C.; Marino, C.; Gasteiger, H. A. Carbon Coating Stability on High-Voltage Cathode Materials in H_2O-Free and H_2O-Containing Electrolyte. *J. Electrochem. Soc.* **2015**, *162*(7), A1227-A1235.

(8) Chung, S.- Y.; Bloking, J. T.; Chiang, Y.- M. Electronically Conductive Phospho-Olivines as Lithium Storage Electrodes. *Nature Mater.* **2002**, *1*, 123-128.

(9) Wang, Z.; Sun, S.; Xia, D.; Chu, W.; Zhang, S.; Wu, Z. Investigation of Electronic Conductivity and Occupancy Sites of Mo Doped into $LiFePO_4$ by ab Initio Calculation and X-ray Absorption Spectroscopy. *J. Phys. Chem. C* **2008**, *112*, 17450-17455.

(10) Ma, Z., Shao, G.; Wang, G.; Du, J.; Zhang, Y. Electrochemical Performance of Mo-Doped $LiFePO_4$/C Composites Prepared by Two-step Solid-State Reaction. *Ionics* **2013**, *19*, 437-443.

(11) Kim, J. C.; Li, X.; Kang, B.; Ceder, G. High-Rate Performance of a Mixed Olivine Cathode with Off-Stoichiometric Composition. *Chem. Commun.* **2015**, *51*, 13279-13282.

(12) Kang, B.; Ceder, G. Battery Materials for Ultrafast Charging and Discharging. *Nature* **2009**, *458*, 190-193.

(13) Herle, P. S.; Ellis, B.; Coombs, N.; Nazar, L. F. Nano-Network Electronic Conduction in Iron and Nickel Olivine Phosphates. *Nature Mater.* **2004**, *3*, 147-152.

(14) Wang, F.; Yang, J.; NuLi, Y.; Wang, J. Highly Promoted

Electrochemical Performance of 5V LiCoPO$_4$ Cathode Material by Addition of Vanadium. *J. Power Sourc*. **2010**, *195*, 6884-6887.

(15) Hausbrand, R.; Cherkashinin, G.; Ehrenberg, H.; Gröting, M.; Albe, K.; Hess, C.; Jaegermann, W. Fundamental Degradation Mechanisms of Layered Oxide Li-Ion Battery Cathode Materials: Methodology, Insights and Novel Approaches. *Mater. Sci. Engineer. B* **2016**, *192*, 3-25.

(16) Wandt, J.; Freiberg, A. T. S.; Ogrodnik, A.; Gasteiger, H. A. Singlet Oxygen Evolution from Layered Transition Metal Oxide Cathode Materials and Its Implications for Lithium-Ion Batteries. *Mater. Today* **2018**, *21*(8), 825-833.

(17) Cherkashinin, G.; Motzko, M.; Schulz, N.; Späth, T.; Jaegermann, W. Electron Spectroscopy Study of Li[Ni,Co,Mn]O$_2$/Electrolyte Interface: Electronic Structure, Interface Composition, and Device Implications. *Chem. Mater*. **2015**, *27*, 2875-2887.

(18) Örnek, A. An Impressive Approach to Solving the Ongoing Stability Problems of LiCoPO$_4$ Cathode: Nickel Oxide Surface Modification with Excellent Core-Shell Principle. *J. Power Sourc*. **2017**, *356*, 1-11.

(19) Örnek, A. The Synthesis of Novel LiNiPO$_4$ Core and Co$_3$O$_4$/CoO Shell Materials by Combining them with Hard-Template and Solvothermal Routes. *J. Coll. Interface Sci*. **2017**, *504*, 468-478.

(20) Lu, Z.; Liu, Y.; Lu, X.; Wang, H.; Yang, G.; Chao, Y.; Li, W.; Yin, F. An Active Core-Shell Nanoscale Design for High Voltage Cathode of Lithium Storage Devices *J. Power Sourc*. **2017**, *360*, 409-418.

(21) Kreder III, K. J.; Manthiram, A. Vanadium-Substituted LiCoPO$_4$ Core with a Monolithic LiFePO$_4$ Shell for High-Voltage Lithium-Ion Batteries. *ACS Energy Lett*. **2017**, *2*, 64-69.

(22) Zhang, Y.; Wang, Z.- B.; Yu, F.- D.; Que, L.- F.; Wang, M.- J.; Xia, Y.- F.; Xue, Y.; Wu, J. Studies on Stability and Capacity for Long-Life Cycle Performance of Li(Ni$_{0.5}$Co$_{0.2}$Mn$_{0.3}$)O$_2$ by Mo Modification for Lithium-Ion Battery. *J. Power Sourc*. **2017**, *358*, 1-12.#

(23) Bai, N.; Ma, Y.- J.; Wang, A.- M.; Luo, X. Effects of MoO$_3$ Coating on the Structure and Electrochemical Performance of High-Voltage Spinel LiNi$_{0.5}$Mn$_{1.5}$O$_4$. *Ionics* **2021**, 27, 469-478.

(24) Wang, J.; Zhao, Y.; Zhang, X.; Wu, H.; Hu, S.; Wei, K.; Cui, Y.; Su, W.; Cui, Y. Trace Molybdenum Doped Li$_2$RuO$_3$ as a Cathode Material with Enhanced Performance for Lithium Ion Batteries. *Sustain. Energy Fuels* **2019**, *3*, 2697-2704.

(25) Cherkashinin, G.; Sharath, S. U.; Jaegermann, W. Toward Enhanced Electronic and Ionic Conductivity in Olivine LiCoPO$_4$ Thin Film Electrode Material for 5 V Lithium Batteries: Effect of

LiCo$_2$P$_3$O$_{10}$ Impurity Phase. *Adv. Energy Mater*. **2017**, *7*, 1602321/1-5.

(26) Oster, M.; Tapp, J.; Hagenow, A.; Möller, A. Thermal oxidation of the intermetallic phases Al$_8$Mo$_3$ and AlMo$_3$. *J. Sol. State Chem*. **2017**, *251*, 233-236.

(27) Son, H. B.; Jeong, M.- Y.; Han, J.- G.; Kim, K.; Kim, K. H.; Jeong, K.- M.; Choi, N.- S. Effect of Reductive Cyclic Carbonate Additives and Linear Carbonate Cosolvents on Fast Chargeability of LiNi$_{0.6}$Co$_{0.2}$Mn$_{0.2}$O$_2$/Graphite Cells. *J. Power Sourc*. **2018**, *400*, 147-156.

(28) Tanuma, S.; Powell, C. J.; Penn, D. R. Calculations of Electron Inelastic Mean Free Paths. V. Data for 14 Organic Compounds over the 50-2000 eV Range. *Surf. Interf. Anal*. **1993**, *21*, 165-176.

(29) Scoefield, J. H. Hartree-Slater Subshell Photoionization Cross-Sections at 1254 and 1487 eV. *J. Electron Spectrosc. Relat Phenom*. **1976**, *8*, 129-137. J. J. Yeh and I. Lindau, *Atomic Data and Nuclear Data Tables*, **1985**, *32*, 1-155.

(30) Giannozzi, P.; *et al*. QUANTUM ESPRESSO: a modular and open-source software project for quantum simulations of materials. *J. Phys. Condens. Matter*. **2009**, *21*, 395502/1-19. Giannozzi, P.; *et al*. Advanced capabilities for materials modelling with Quantum ESPRESSO. *J. Phys. Condens. Matter*. **2017**, *29*, 465901.

(31) Perdew, J. P.; Ruzsinszky, A.; Csonka, G. I.; Vydrov, O. A.; Scuseria, G. E.; Constantin, L. A.; Zhou, X.; Burke, K. Restoring the Density-Gradient Expansion for Exchange in Solids and Surfaces. *Phys. Rev. Lett*. **2008**, *100*, 136406/1-4.

(32) Zhou, F.; Cococcioni, M.; Marianetti, A. C.; Morgan, D.; Ceder, G. First-principles prediction of redox potentials in transition-metal compounds with LDA+U. *Phys. Rev. B* **2004**, *70*, 235121/1-8. Zhou, F.; Cococcioni, M.; Kang, K.; Ceder, G. The Li intercalation potential of LiMPO$_4$ and LiMSiO$_4$ olivines with M = Fe, Mn, Co, Ni. *Electrochem. Communicat*. **2004**, *6*, 1144-1148. Zhou, F.; Marianetti, A. C.; Cococcioni, M.; Morgan, D.; Ceder, G. Phase separation in Li$_x$FePO$_4$ induced by correlation effects. *Phys. Rev. B* **2004**, *69*, 201101/1-4. Liu, X.; *et al*. Phase Transformation and Lithiation Effect on Electronic Structure of Li$_x$FePO$_4$: An In-Depth Study by Soft X-ray and Simulations. *J. Am. Chem. Soc*. **2012**, *134*, 13708-13715. Garcia- Lastra, J.- M.; Myrdal, J. S. G.; Thygesen, K. S.; Vegge, T. DFT+U Study of Polaronic Conduction in Li$_2$O$_2$ and Li$_2$CO$_3$: Implications for Li–Air Batteries. *J. Phys. Chem. C* **2013**, *117*, 5568-5577; Barbiellini, B.; Kuriplach, J. Advanced characterization of lithium battery materials with positrons. *J. Phys. Conf. Series* **2017**, *791*, 012016/1-6. Hafiz, H.; *et al*. Visualizing redox orbitals

and their potentials in advanced lithium-ion battery materials using high-resolution x-ray Compton scattering. *Science Adv*. **2017**, *3*, e1700971/1-6. Hautier, G. Prediction of New Battery Materials Based on Ab initio Computations. *AIP Conf. Proceed* **2016**, *1765*, 020009/1-10.

(33) Timrov, I.; Marzari, N.; Cococcioni, M. Hubbard parameters from density functional perturbation theory. *Phys. Rev. B* **2018**, *98*, 085127/1-15. Timrov, I.; Marzari, N.; Cococcioni, M. Self-consistent Hubbard parameters from density-functional perturbation theory in the ultrasoft and projector-augmented wave formulations. *Phys. Rev. B* **2021**, *103*, 045141/1-14.

(34) Cococcioni, M.; Marzari, N. Energetics and cathode voltages of $LiMPO_4$ olivines (M = Fe, Mn) from extended Hubbard functionals. *Phys. Rev. Mat*. **2019**, *3*, 033801/1-22.

(35) Stavitski, E.; de Groot, F. M. F. The CTM4XAS program for EELS and XAS spectral shape analysis of transition metal L edges. *Micron* **2010**, *41*, 687-694.

(36) de Groot, F. M. F.; Abbate, M.; van Elp, J.; Sawatzky, G. A.; Ma, Y. J.; Chen, C. T.; Sette, F. Oxygen 1s and Cobalt 2p X-ray Absorption of Cobalt Oxides. *J. Phys. Condens. Matter*. **1993**, *5*, 2277-2288.

(37) Haverkort, M. W.; Hu, Z.; Cezar, J. C.; Burnus, T.; Hartmann, H.; Reuther, M.; Zobel, C.; Lorenz, T.; Tanaka, A.; Brookes, N. B.; Hsieh, H. H.; Lin, H.- J.; Chen, C. T.; Tjeng, L. H. Spin State Transition in $LaCoO_3$ Studied Using Soft X-ray Absorption Spectroscopy and Magnetic Circular Dichroism. *Phys. Rev. Lett*. **2006**, *97*, 176405/1-4.

(38) Saitoh, T.; Mizokawa, T.; Fujimori, A.; Abbate, M.; Takeda, Y.; Takano, M. Electronic structure and temperature-induced paramagnetism in $LaCoO_3$. *Phys. Rev. B* **1997**, *55*, 4257-4266

(39) Gerischer, H.; Decker, F.; Scrosati, B. The Electronic and the Ionic Contribution to the Free Energy of Alkali Metals in Intercalation Compounds. *J Electrochem. Soc*. **1994**, *141*(9), 2297-2300.

(40) Owen, J. R. Rechargeable Lithium Batteries. Chem. *Soc. Rev*. **1997**, *26*, 259-267.

(41) Cherkashinin, G.; Hausbrand, R.; Jaegermann, W. Performance of Li-Ion Batteries: Contribution of Electronic Factors to the Battery Voltage *J. Electrochem. Soc*. **2019**, *166*(3), A5308-A5312.

(42) Le Bacq, O.; Pasturel, A.; Bengone, O. Impact on Electronic Correlations on the Structural Stability, Magnetism, and Voltage of $LiCoPO_4$ Battery. *Phys. Rev. B* **2004**, *69*, 245107/1-9.

(43) Cherkashinin, G.; Lebedev, M. V.; Sharath, S. U.; Hajduk, A.; Nappini, S.; Magnano, E. Exploring Redox Activity in a $LiCoPO_4$–

$LiCo_2P_3O_{10}$ Tailored Positive Electrode for 5 V Lithium Ion Batteries: Rigid Band Behavior of the Electronic Structure and Stability of the Delithiated Phase. *J. Mater. Chem. A* **2018**, *6*, 4966-4970.

(44) Amine, K.; Yasuda, H.; Yamachi, M. Olivine $LiCoPO_4$ as 4.8 V Electrode Material for Lithium Batteries. *Electrochem. Solid State Lett*. **2000**, *3*, 178-179.

(45) Ludwig, J.; Alarcón-Suesca, C.; Geprägs, S.; Nordlund, D.; Doeff, M. M.; Orench, I. P.; Nilges, T. Direct Synthesis and Characterization of Mixed Valent $Li_{0.5-\delta}CoPO_4$, a Li-Deficient Derivative of the *Cmcm* Polymorph of $LiCoPO_4$. *RSC Adv*. **2017**, 7, 28069-28081.

(46) Jaegermann, W.; Mayer, Th. Surface Science Studies of Elementary Processes in Photo-Electrochemistry: Adsorption of Electrolyte Components on Layered Transition Metal Dichalcogenides. *Solar Energy Mat. Sol. Cells* **2004**, *83*, 371-394.

(47) Cherkashinin, G.; Krischok, S.; Himmerlich, M.; Ambacher, O.; Schaefer, J. A. Electronic Properties of C_{60}/InP(001) Heterostructures. *J. Phys.: Condens. Matter*. **2006**, *18*, 9841-9848.

(48) Thißen, A.; Ensling, D.; Liberatore, M.; Wu, Q.-H.; Madrigal, F. J. F.; Bhuvaneswari, M. S.; Hunger, R.; Jaegermann, W. Experimental Routes to In Situ Characterization of the Electronic Structure and Chemical Composition of Cathode Materials for Lithium Ion Batteries during Lithium Intercalation and Deintercalation using Photoelectron Spectroscopy and Related Techniques. *Ionics* **2009**, *15*, 393-403.

(49) Schulz, N.; Hausbrand, R.; Dimesso, L.; Jaegermann, W. XPS-Surface Analysis of SEI Layers on Li-Ion Cathodes: Part I. Investigation of Initial Surface Chemistry. *J. Electrochem. Soc*. **2018**, *165*(5), A819-A832.

(50) Lapping, J. G.; Delp, S. A.; Allen, J. L.; Allen, J. L.; Freeland, J. W.; Johannes, M. D.; Hu, L.; Tran, D. T.; Jow, T. R.; Cabana, J. Changes in Electronic Structure upon Li Deintercalation from $LiCoPO_4$ Derivatives. *Chem. Mater*. **2018**, *30*, 1898-1906.

(51) Saitoh, M.; Gao, X.; Ogawa, T.; Ikuhara, Y. H.; Kobayashi, S.; J. Fisher, C. A.; Kuwabara, A.; Ikuhara, Y. Systematic Analysis of Electron Energy-Loss Near-Edge Structures in Li-Ion Battery Materials. *Phys. Chem. Chem. Phys*. **2018**, *20*, 25052-25061.

(52) Nakayama, M.; Goto, S.; Uchimoto, Y.; Wakihara, M.; Kitajima, Y. Changes in Electronic Structure between Cobalt and Oxide Ions of Lithium Cobalt Phosphate as 4.8-V Positive Electrode Material. *Chem. Mater*. **2004**, *16*, 3399-3401.

(53) Augustsson, A.; Zhuang, G. V.; Butorin, S. M.; Osorio-Guillén, J. M.; Dong, C. L.; Ahuja, R.; Chang, C. L.; Ross, P. N.; Nordgren, J.; Guo, J.-H. Electronic Structure of Phospho-Olivines Li_xFePO_4 (x=0,

1) from Soft-X-Ray- Absorption and -Emission Spectroscopies. *J. Chem. Phys*. **2005**, *123*, 184717/1-9.

(54) Zhou, J.; Wang, J.; Zuin, L.; Regier, T.; Hu, Y.; Wang, H.; Liang, Y.; Maley, J.; Sammynaiken, R.; Dai, H. Spectroscopic Understanding of Ultra- High Rate Performance for LiMn$_{0.75}$Fe$_{0.25}$PO$_4$ Nanorods– Graphene Hybrid in Lithium Ion Battery. *Phys. Chem. Chem. Phys*. **2012**, *14*, 9578-9581.

(55) Frati, F.; Hunault, M. O. J. Y.; de Groot, F. M. F. Oxygen K-edge X-ray Absorption Spectra. *Chem. Rev*. **2020**, *120*, 4056-4110.

(56) Cherkashinin, G.; Jaegermann, W. Dissociative Adsorption of H$_2$O on LiCoO$_2$ (00*l*) Surfaces: Co Reduction Induced by Electron Transfer from Intrinsic Defects. *J. Chem. Phys*. **2016**, *144*, 184706/1-7.

(57) Kinyanjui, M. K.; Axmann, P.; Wohlfahrt-Mehrens, M.; Moreau, P.; Boucher, F.; Kaiser, U. Origin of Valence and Core Excitations in LiFePO$_4$ and FePO$_4$. *J. Phys. Condens. Matter*. **2010**, *22*, 275501/1-8.

(58) Schuster, M. E.; Teschner, D.; Popovic, J.; Ohmer, N.; Girgsdies, F.; Tornow, J.; Willinger, M. G.; Samuelis, D.; Titirici, M.-M.; Maier, J.; Schlögl, R. Charging and Discharging Behavior of Solvothermal LiFePO$_4$ Cathode Material Investigated by Combined EELS/NEXAFS Study. *Chem. Mater*. **2014**, *26*, 1040-1047.

(59) Yin, Z.; Kasrai, M.; Bancroft, G. M.; Tan, K. M.; Feng, X. X-ray-Absorption Spectroscopic Studies of Sodium Polyphosphate Glasses. *Phys. Rev. B* **1995**, *51*, 742-750.

(60) Kruse, J.; Leinweber, P.; Eckhardt, K.- U.; Godlinski, F.; Hu, Y.; Zuin, L. Phosphorus L$_{2,3}$-edge XANES: Overview of Reference Compounds. *J. Synchrotron Rad*. **2009**, *16*, 247-259.

(61) Nakayama, M.; Goto, S.; Uchimoto, Y.; Wakihara, M.; Kitajima, Y.; Miyanaga, T.; Watanabe, I. X-ray Absorption Spectroscopic Study on the Electronic Structure of Li$_{1-x}$CoPO$_4$ Electrodes as 4.8 V Positive Electrodes for Rechargeable Lithium Ion Batteries. *J. Phys. Chem. B* **2005**, *109*, 11197-11203.

(62) Zhang, Z.; Hu, L.; Wu, H.; Weng, W.; Koh, M.; Redfern, P.C.; Curtiss, L.A.; Amine, K. Fluorinated Electrolytes for 5 V Lithium-Ion Battery Chemistry. *Energy Environ Sci*. **2013**, *6*, 1806-1810.

(63) Schwenke, K. U.; Solchenbach, S.; Demeaux, J.; Lucht, B. L.; Gasteiger, H. A. The Impact of CO$_2$ Evolved from VC and FEC during Formation of Graphite Anodes in Lithium-Ion Batteries. *J. Electrochem. Soc*. **2019**, *166*(10), A2035-A2047.

(64) Lee, S. Y.; Park, Y. J. Effect of Vinylethylene Carbonate and Fluoroethylene Carbonate Electrolyte Additives on the Performance of Lithia-Based Cathodes. *ACS Omega* **2020**, *5*, 3579-3587.

(65) Xia, L.; Lee, S.; Jiang, Y.; Xia, Y.; Chen, G. Z.; Liu, Z. Fluorinated Electrolytes for Li-Ion Batteries: The Lithium Difluoro(oxalato)borate Additive for Stabilizing the Solid Electrolyte Interphase. *ACS Omega* **2017**, *2*, 8741-8750.

(66) Zhu, Y.; Wang, J.; Zhang, F.; Gao, S.; Wang, A.; Fang, W.; Jin, J. Zwitterionic Nanohydrogel Grafted PVDF Membranes with Comprehensive Antifouling Property and Superior Cycle Stability for Oil-in-Water Emulsion Separation. *Adv. Funct. Mater*. **2018**, *28*, 1804121/1-10.

(67) Cherkashinin, G.; Schuch, J.; Kaiser, B.; Alff, L.; Jaegermann, W. High Voltage Electrodes for Li-Ion Batteries and Efficient Water Electrolysis: An Oxymoron? *J. Phys. Chem. Lett*. **2020**, *11*, 3754-3760.

(68) Kim, K.; Park, I.; Ha, S.- Y.; Kim, Y.; Woo, M.- H.; Jeong, M.-H.; Shin, W. C.; Ue, M.; Hong, S. Y.; Choi, N.- S. Understanding the Thermal Instability of Fluoroethylene Carbonate in LiPF$_6$-based Electrolytes for Lithium Ion Batteries. *Electrochim. Acta* **2017**, *225*, 358-368.

(69) Xu, C.; Lindgren, F.; Philippe, B.; Gorgoi, M.; Bjöefors, F.; Edström, K.; Gustafsson, T. Improved Performance of the Silicon Anode for Li-Ion Batteries: Understanding the Surface Modification Mechanism of Fluoroethylene Carbonate as an Effective Electrolyte Additive. *Chem. Mater*. **2015**, *27*, 2591-2599.

(70) Zhu, Y.; Pande, V.; Lia, L.; Wen, B.; Pan, M. S.; Wang, D.; Ma, Z.- F.; Viswanathan, V.; Chiang, Y.- M. Design Principles for Self-forming Interfaces Enabling Stable Lithium-Metal Anodes. *PNAS* **2020**, *117*(44), 27195-27203.

(71) Markevich, E.; Salitra, G.; Fridman, K.; Sharabi, R.; Gershinsky, G.; Garsuch, A.; Semrau, G.; Schmidt, M. A.; Aurbach, D. Fluoroethylene Carbonate as an Important Component in Electrolyte Solutions for High-Voltage Lithium Batteries: Role of Surface Chemistry on the Cathode. *Langmuir* **2014**, *30*, 7414-7424.

(72) Nie, M.; Demeaux, J.; Young, B. T.; Heskett, D. R.; Chen, Y.; Bose, A.; Woicik, J. C.; Lucht, B. L. Effect of Vinylene Carbonate and Fluoroethylene Carbonate on SEI Formation on Graphitic Anodes in Li-Ion Batteries. *J. Electrochem. Soc*. **2015**, *162*(13), A7008-A7014.

(73) Xia, L.; Tang, B.; Yao, L.; Wang, K.; Cheris, A.; Pan, Y.; Lee, S.; Xia, Y.; Chen, G. Z.; Liu, Z. Oxidation Decomposition Mechanism of Fluoroethylene Carbonate-Based Electrolytes for High-Voltage Lithium Ion Batteries: A DFT Calculation and Experimental Study. *ChemistrySelect* **2017**, *2*, 7353-7361.

(74) Zheng, Q.; Yamada, Y.; Shang, R.; Ko, S.; Lee, Y.- Y.; Kim, K.; Nakamura, E.; Yamada, A. A Cyclic Phosphate-based Battery

Electrolyte for High Voltage and Safe Operation. *Nature Energy* **2020**, *5*, 291-298.

(75) Veith, G. M.; Doucet, M.; Sacci, R. L.; Vacaliuc, B.; Baldwin, J. K.; Browning, J. F. Determination of the Solid Electrolyte Interphase Structure Grown on a Silicon Electrode Using a Fluoroethylene Carbonate Additive. *Sci. Reports* **2017**, *7*, 6326/1-15.

(76) Kumar, V.; Wang, X.; Lee, P. S. Formation of Hexagonal-Molybdenum Trioxide (h-MoO$_3$) Nanostructures and their Pseudocapacitive Behavior. *Nanoscale* **2015**, *7*, 11777-11786.

(77) Powell, J. M. Metal Oxyhalides and Halides for use as Electrode Materials in Li-Ion Batteries. PhD, **2017.** The University of Tennessee, Knoxville.

(78) Scanlon, D. O.; Watson, G. W.; Payne, D. J.; Atkinson, G. R.; Egdell, R. G.; Law, D. S. L. Theoretical and Experimental Study of the Electronic Structures of MoO$_3$ and MoO$_2$. *J. Phys. Chem. C* **2010**, *114,* 4636-4645.

(79) Liao, X.; Jeong, A. R.; Wilks, R. G.; Wiesner, S.; Rusu, M.; Bär, M. X-ray Irradiation Induced Effects on the Chemical and Electronic Properties of MoO$_3$ Thin Films. *J. Electron Spectrosc. Relat. Phenom*. **2016**, *212*, 50-55.

(80) Szymanska, A.; Nitek, W.; Oszajca, M.; Łasocha, W.; Pamin, K.; Połtowicz, J. Molybdenum Complexes as Catalysts for the Oxidation of Cycloalkanes with Molecular Oxygen. *Catal. Lett*. **2016**, *146,* 998-1010.

(81) Spencer, N. D.; Pereira, C. J. Partial Oxidation of CH$_4$ to HCHO over a MoO$_3$-SiO$_2$ Catalyst: A Kinetic Study *AIChE J*. **1987**, *33*(11), 1808-1812.

(82) Raun, K. V.; Lundegaard, L. F.; Beato, P.; Appel, C. C.; Nielsen, K.; Thorhauge, M.; Schumann, M.; Jensen, A. D.; Grunwaldt, J.- D.; Hoj, M. Stability of Iron-Molybdate Catalysts for Selective Oxidation of Methanol to Formaldehyde: Influence of Preparation Method. *Catal. Lett*. **2020**, *150*, 1434-1444.

(83) Zhang, T.; Yang, X.; Ge, Q. Surface Chemistry and Reactivity of α-MoO$_3$ Toward Methane: A SCAN-Functional Based DFT Study. *J. Chem. Phys*. **2019**, *151*, 044708/1-8.

(84) Popov, B. I.; Bibin, V. N.; Boreskov, G. K. Study of an Ironmolybfate Oxide Catalyst for Oxidation of Methanol to Formaldehyde. *Kinet. Catal*. **1976**, *17*, 322-327.

(85) Rinkel, B. L. D.; Hall, D. S.; Temprano, I.; Grey, C. P. Electrolyte Oxidation Pathways in Lithium-Ion Batteries. *J. Am. Chem. Soc*. **2020**, *142*, 15058-15074.

(86) Solchenbach, S.; Metzger, M.; Egawa, M.; Beyer, H.; Gasteiger, H. A. Quantification of PF$_5$ and POF$_3$ from Side Reactions of LiPF$_6$ in Li-Ion Batteries. *J. Electrochem. Soc*. **2018**, *165*(13), A3022-A3028.

(87) Borodin, O.; Behl, W.; Jow, T. R. Oxidative Stability and Initial Decomposition Reactions of Carbonate, Sulfone, and Alkyl Phosphate-Based Electrolytes. *J. Phys. Chem. C* **2013**, *117*, 8661-8682.

(88) Fan, X.; Chen, L.; Borodin, O.; Ji, X.; Chen, J.; Hou, S.; Deng, T.; Zheng, J.; Yang, C.; Liou, S.- C.; Amine, K.; Xu, K.; Wang, C. Non-Flammable Electrolyte Enables Li-Metal Batteries with Aggressive Cathode Chemistries. *Nat. Nanotech*. **2018**, *13*, 715-722.

(89) Borgschulte, A.; Sambalova, O.; Delmelle, R.; Jenatsch, S.; Hany, R.; Nüesch, F. Hydrogen Reduction of Molybdenum Oxide at Room Temperature. *Sci. Reports* **2017**, 7, 40761/1-9.

(90) Borodin, O. Challenges with Prediction of Battery Electrolyte Electrochemical Stability Window and Guiding the Electrode–Electrolyte Stabilization. *Curr. Opin. Electrochem*. **2019**, *13*, 86-93.

(91) Kühn, M.; Mankel, E.; Köhn, A.; Mayer, T.; Jaegermann, W. Doping Mechanism of MoO$_3$ in 4,4´-Bis(*N*-carbazolyl)-1,1´-biphenyl: A Photoelectron Spectroscopic Study. *Phys. Status Sol. B* **2016**, *253*(9), 1697-1706.
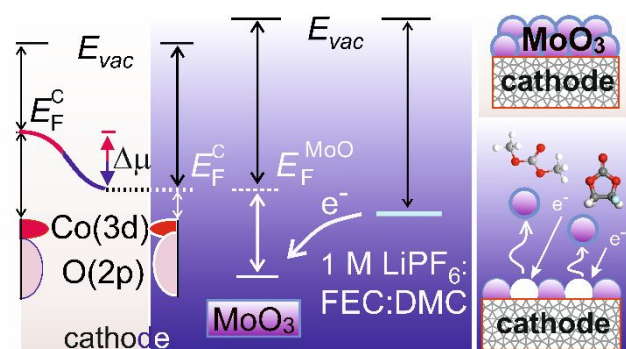

Table of Contents (TOC)

Supporting Information

Energy Level Alignment at Cobalt Phosphate/Electrolyte Interface: Intrinsic Stability vs. Interfacial Chemical Reactions in 5 V Lithium Ion Batteries

Gennady Cherkashinin [a,*], Robert Eilhardt,[a] Silvia Nappini,[b] Matteo Cococcioni,[c] Igor Píš,[b,d] Simone dal Zilio,[b] Federica Bondino,[b] Nicola Marzari,[e] Elena Magnano[b,f] and Lambert Alff [a]

[a] Institute of Materials Science, Technische Universität Darmstadt, Alarich-Weiss-Str. 2, D-64287 Darmstadt, Germany
[b] IOM CNR Laboratorio TASC, Strada Statale 14, km. 163,5 in Area Science Park, 34149 Basovizza, Trieste, Italy
[c] Physics Department, University of Pavia, Via Bassi 6, I-27100 Pavia, Italy
[d] Elettra - Sincrotrone Trieste S.C.p.A., Basovizza, TS, Italy
[e] Theory and Simulation of Materials (THEOS), and National Centre for Computational Design and Discovery of Novel Materials (MARVEL), Ecole Polytechnique Federale de Lausanne (EPFL), CH-1015 Lausanne, Switzerland
[f] Department of Physics, University of Johannesburg, PO Box 524, Auckland Park, 2006, Johannesburg, South Africa

To whom the correspondence should be addressed:
* E-mail: gennady.cherkashinin@tu-darmstast.de
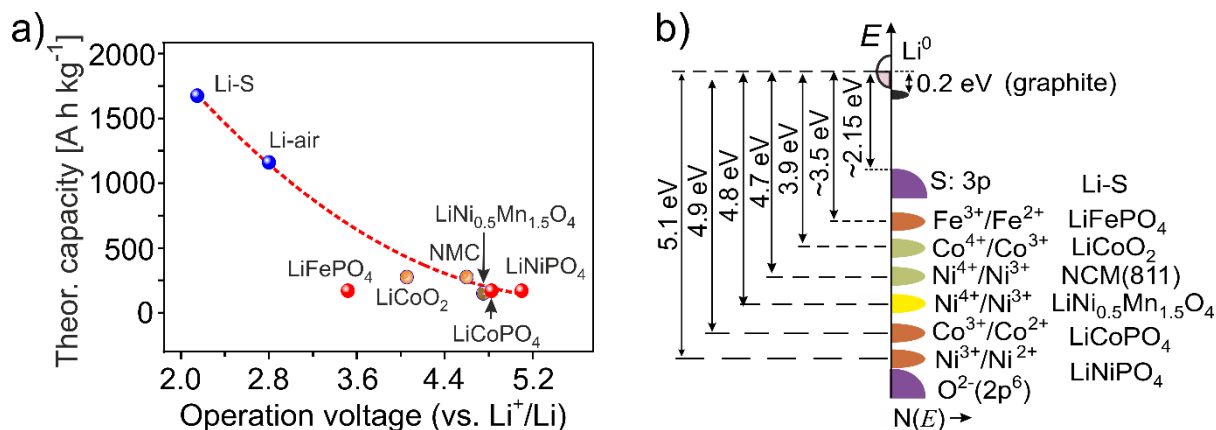
Figure S1. a) The theoretical capacity of various cathode materials vs. average operation voltage of battery cells. b) The electrochemical potentials, $\mu_{e^-}^C$, vs. lithium of the cathode materials with major interest for commercial application. NCM(811) $\equiv$ LiNi$_{0.8}$Co$_{0.1}$Mn$_{0.1}$O$_2$.
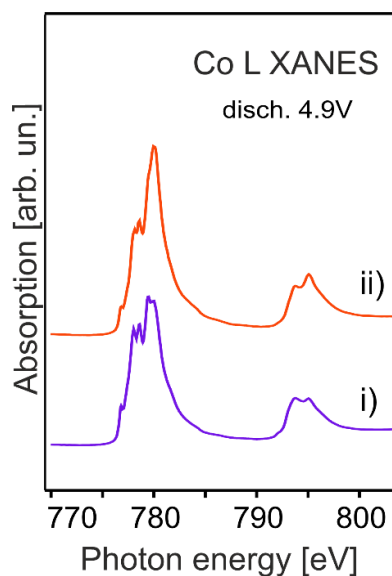
Figure S2. Co L- edge XANES of the LCP–LCPO cathode material discharged to 4.9 V vs. Li$^+$/Li. The blue (i) and red (ii) are the spectra measured at different areas of the thin film. A higher intensity of the high energy shoulder in the upper spectrum (ii) evidences that more Co^{2+} ions are oxidized to the Co^{3+} state, as compared to (i). The spectra were collected in total electron yield (TEY) mode.
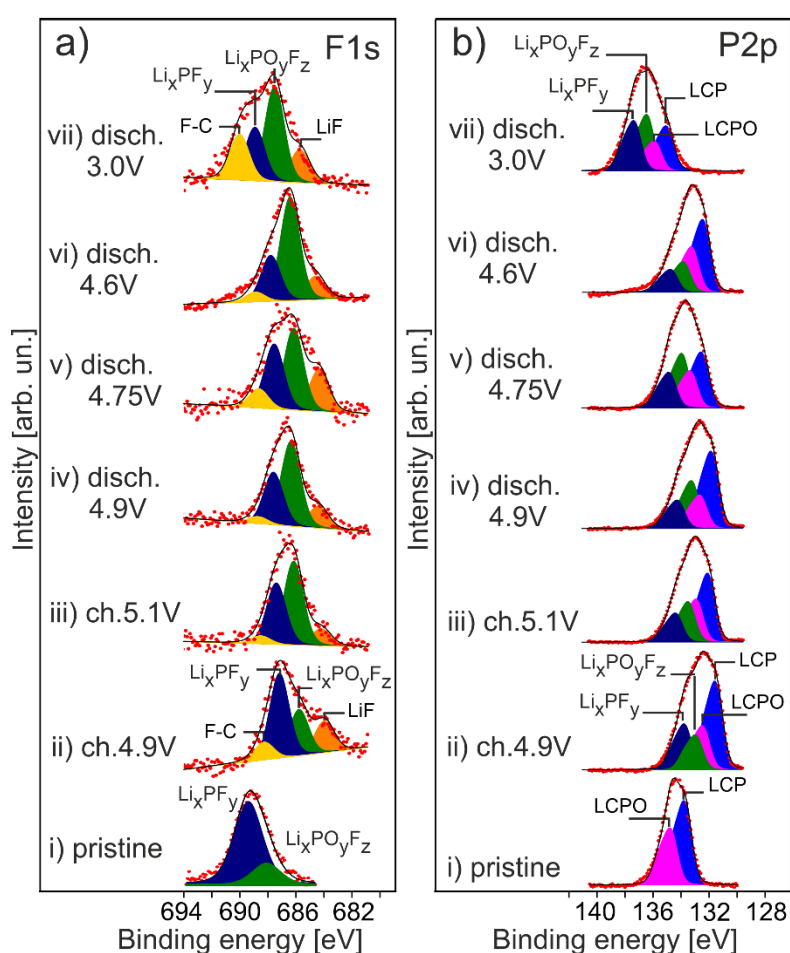

Figure S3. a) F 1s (hν=1457 eV)- and b) P 2p (hν=875 eV) photoemission core- level spectra measured of the LCP–LCPO cathode material: pristine (after storing in a glove-box) (i); charging states of 4.9 V (ii) and 5.1 V (iii); discharging states of 4.9 V (iv), 4.75 V (v); 4.6 V (vi) and 3.0 V (cycled) (vii). The probing depth, d=3λ(E_{kin}), is ~70 Å.
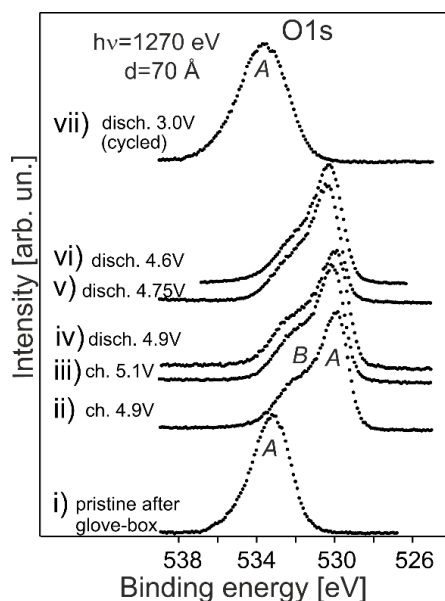
Figure S4. Evolution of the O 1s (hν=1270 eV)- core-level spectra vs. charging/discharging the LCP−LCPO thin film cathode material: pristine (i), charged to 4.9V (ii) and 5.1V (iii) vs. Li$^+$/Li; discharged to 4.9V (iv), 4.75V (v), 4.65V (vi) and 3.0 V (cycled, (vii)) vs. Li$^+$/Li. The probing depth is ~70 Å. a) The *A* spectral feature is associated with the lattice oxygen, The shoulder *B* at higher binding energy is "non-stoichiometric" oxygen, mostly associated with PO$_y$F$_z$ due to the electrolyte decomposition upon electrochemical cycle.
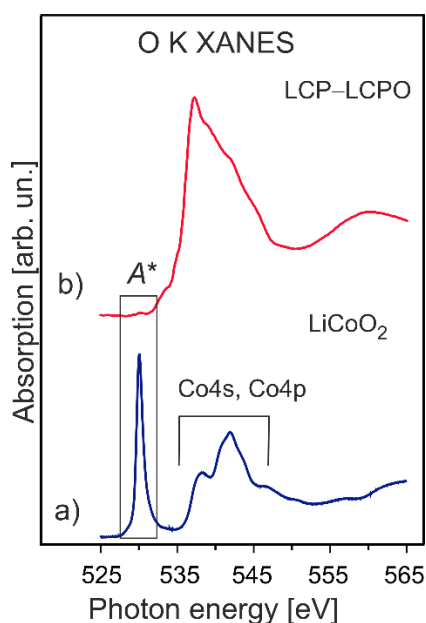
Figure S5. O K- edge XANES of the LiCoO$_2$ layered- (a) and LCP −LCPO (b) structure materials. The sharp feature *A** corresponds to the electron transition from occupied O 1s core level to empty O 2p − Co 3d hybrid states. The oxygen 2p states are highly hybridized with Co 3d (e$^*_g$) states, thereby leading mostly to 3d character of these empty bands. The broad structure above 5 eV is attributed to transitions into O 2p states hybridized with Co 4s and Co 4p states.
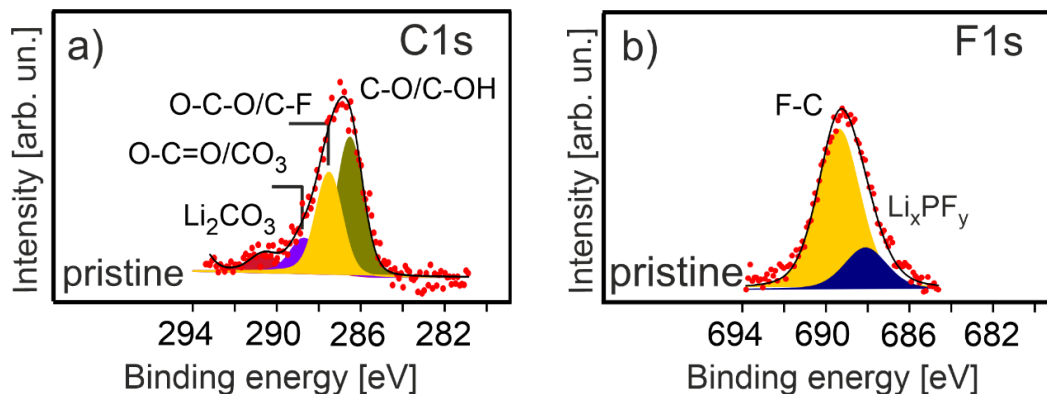
Figure S6. a) C 1s (hν=1020 eV)- and b) F 1s (hν=870 eV)- photoemission core- level spectra of the LCP−LCPO stored first in a glove-box and then in UHV conditions for several days. The probing depth is ~70 Å (a) and 25 Å (b), respectively. The C 1s photoelectron line is fitted by four components assigned to C−OH/C−O (286.5 eV), C−O−C/C−F (287.7 eV), O−C=O (288.5 eV) and Li_2CO_3 (290.6 eV). The F 1s photoelectron spectrum is fitted by two spectral components: F−C (689.2 eV) and Li_xPF_y (688.1 eV). The Li_xPF_y binding energy is in a good agreement with the value reported for the $LiCoPO_4$ composite material (Ref.[15])
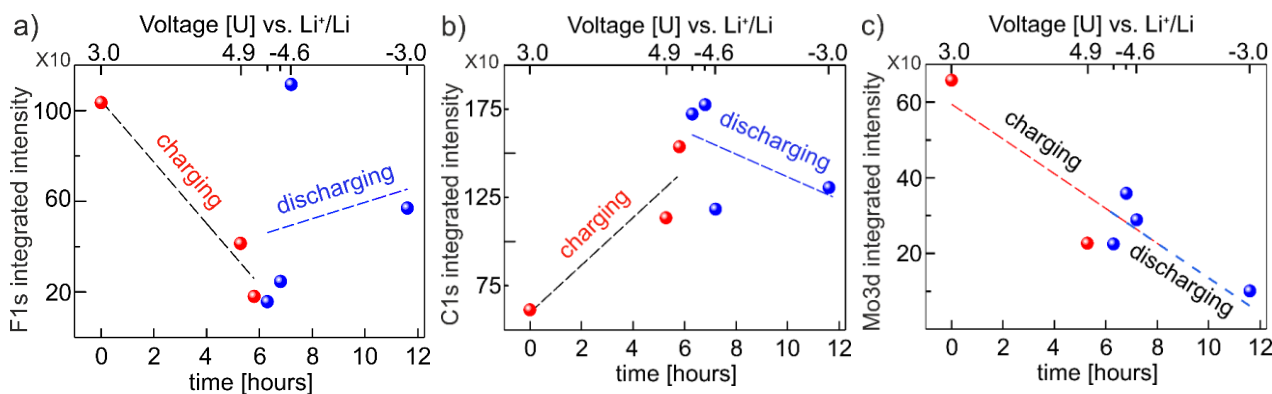
Figure S7. The evolution of F 1s (a), C 1s (b) and Mo 3d (c) photoemission intensities vs. electrochemical charging/discharging of the LCP-LCPO cathode. Charged- and discharged- states are shown in red- and blue- solid circles, respectively. The lower x- axis is the time to reach a specific charging- and discharging potential, respectively. The upper x-axis is the voltage potential applied to the LCP−LCPO battery cell.
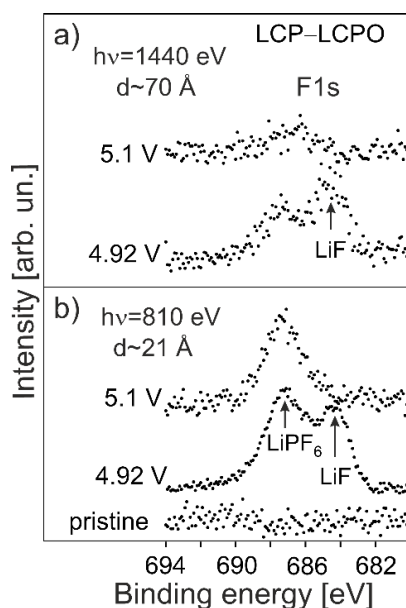
Figure S8. F 1s photoemission core-level spectra of the LCP−LCPO/ electrolyte interface yielded at two different probing depths: a) ~70 Å (hν=1440 eV, the electron's IMFP λ~ 22.5 Å) and b) ~21 Å (hν= 810 eV, λ~7 Å) and vs. a charging state of 4.92 V, 5.1 V.
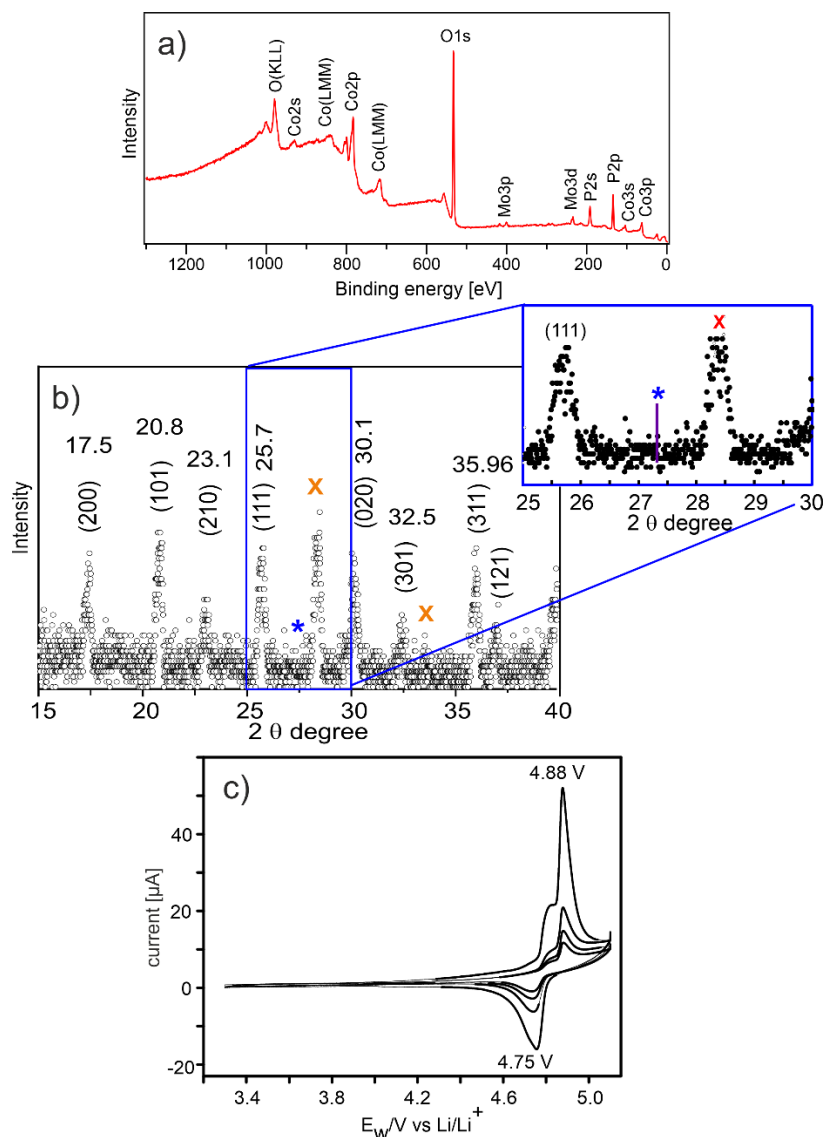

Figure S9. a LCP-LCPO thin film cathode material coated with MoO_3 (pristine sample): a) X-ray photoelectron survey spectrum (hυ=1486.7 eV); b) the XRD pattern indexed to a olivine $LiCoPO_4$ of *Pnma* space group symmetry (the ICSD No. 01-078-5576). $LiCo_2P_3O_{10}$ of $P2_1/m$(11) space group symmetry (the ICSD No. 04-011-4098) is shown by cross (X). No patterns related to the MoO_3 crystallographic phase are detected. The inset shows the 2θ region with the expected most intense (100) peak at 2θ=27.33 from MoO_3 (the ICSD No. 00-005-0508), denoted by the blue vertical line and star (*); c) after several electrochemical cycles by using cyclic voltammetry.
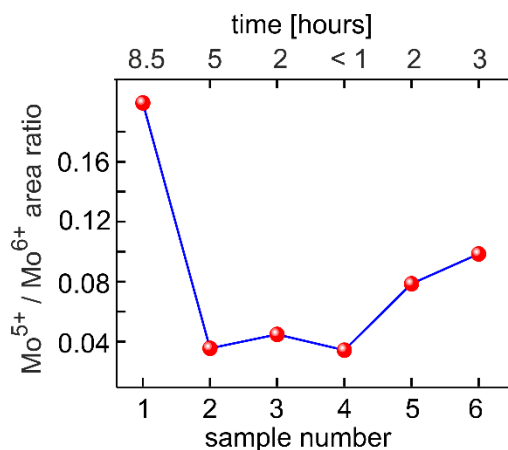
Figure S10. The Mo^{5+}/ Mo^{6+} ratio vs time of X-ray beam exposure during the synchrotron measurements. It evidences that the reduction of Mo(VI) to Mo(V) during charging/discharging LCP−LCPO is mostly determined by the intrinsic interface properties, but not due to X-ray beam damage. The peak areas were estimated from the fitted Mo3d spectra (Figure 4c) normalized to the maximum intensity. (1) LCP−LCPO pristine (after storing in a glove box); (2) charged to 4.9 V; (3) discharged to 4.9 V; (4) discharged to 4.75 V; (5) discharged to 4.6 V; (6) discharged to 3.0 V (after 1st electrochemical cycle).
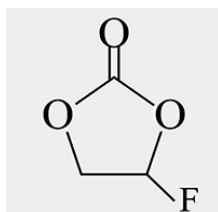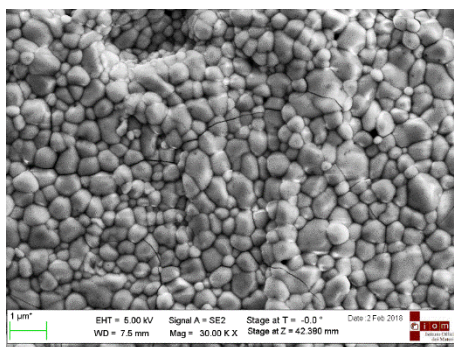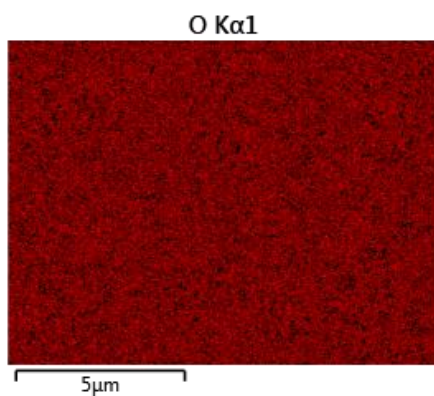

Figure S11. Chemical structure of fluoroethylene carbonate (FEC): C$_3$H$_3$FO$_3$.

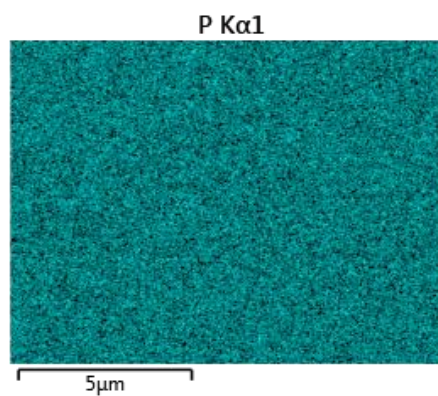**a)**

b)

O Kα1

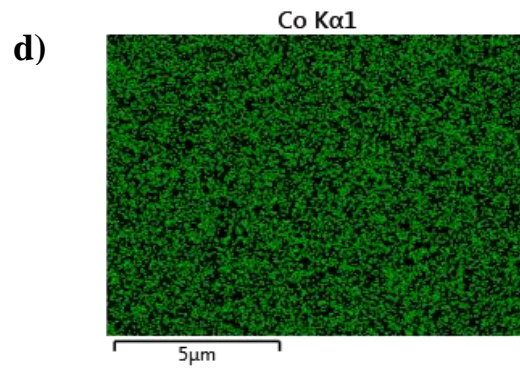**c)**

P Kα1

d)

Co Kα1

5μm

Figure S12. SEM image (a) and EDS maps (b-d) of a LCP−LCPO with a thin MoO$_3$ layer on the top. The sample is homogeneous in crystals size, shape and distribution.

REFERENCES

(1 S) Markevich, E.; Salitra, G.; Fridman, K.; Sharabi, R.; Gershinsky, G.; Garsuch, A.; Semrau, G.; Schmidt, M. A.; Aurbach, D. Fluoroethylene Carbonate as an Important Component in Electrolyte Solutions for High-Voltage Lithium Batteries: Role of Surface Chemistry on the Cathode. *Langmuir* **2014**, *30*, 7414-7424.